2014

# Piezospectroscopic Calibration of Alumina-Nanocomposites for the Development of Stress-Sensing Structures

Daniela Fugon-Dessources
*University of Central Florida*

# Piezospectroscopic Calibration of Alumina-Nanocomposites for the Development of Stress-Sensing Structures

by

Daniela Fugon-Dessources
B.S. North Carolina State University, 2012

A thesis submitted in partial fulfillment of the requirements
for the degree of Master of Science
in the Department of Mechanical and Aerospace Engineering
in the College of Engineering and Computer Science
at the University of Central Florida
Orlando, Florida

Spring Term
2014

Major Professor:
Seetha Raghavan

# Abstract

Alpha-alumina is known to exhibit photo-luminescent (PL) properties, mainly characteristic R-lines that shift according to applied stress. In addition to showing excellent PL properties, polymers with embedded alumina nanoparticles have been shown to improve the overall composite mechanical properties. While the use of the PL properties to develop stress-sensing materials using an alumina-epoxy material has been successfully shown in compression, the properties have not been developed for tension. In this study, the PL response of variable volume fraction alumina-epoxy composites will be determined under tensile conditions. It is expected that increasing the volume fraction of alumina nanoparticles will increase the sensitivity of the particles PL emission shift to applied stress. Three tensile alumina-epoxy specimens of 21.0%, 31.2%, and 34.5% volume fractions were manufactured and tested under tensile static loads. The results of this experiment will determine the piezospectroscopic (PS) coefficient and calibration of bulk alumina nanocomposites in tension. A linear region was identified in the PS response of the nanocomposite to the applied tensile load. The PS coefficient of this linear region increased as the volume fraction of the nanocomposite increased. To demonstrate the application of structural composites with stress sensing capabilities, alumina nanoparticles were integrated in the manufacturing of a carbon fiber composite specimen. The results of the stress-sensing composite mechanical experiment showed that alumina nanoparticles were able to detect changes in stress. The results for both the bulk nanocomposite

calibrations and the application of stress-sensing alumina nanoparticles in a carbon-fiber composite will advance the development of this novel stress-sensing method.

*This work is dedicated to my husband, my parents, and my sisters, without your love and support I would not be where I am today*

# Acknowledgments

I would like to thank my committee members, Dr. Raghavan, Dr. Orlovskaya, and Dr. Gou for their expertise and advice. I would also like to thank all of my fellow collaborators and lab mates, especially Ashley Jones. This material is based on work supported by the National Science Foundation under Grant CMMI 1130837 and the University of Central Florida Office of Research and Commercialization Inhouse Grant FY 2012.

TABLE OF CONTENTS

LIST OF FIGURES . . . . . xi

LIST OF TABLES . . . . . xiii

CHAPTER 1 INTRODUCTION . . . . . 1

1.1 Motivation and Background . . . . . 1

1.2 Effects of Nano-Sized Modifiers in Epoxy . . . . . 3

1.3 Micromechanics of Nanocomposites . . . . . 4

1.4 Overview of Research . . . . . 6

CHAPTER 2 PHOTO-LUMINESCENCE, PIEZOSPECTROSCOPY, AND DECONVOLUTION . . . . . 8

2.1 Theory of $\alpha$-Alumina Photo-luminescence . . . . . 8

2.2 Piezospectroscopy . . . . . 9

2.2.1 PS Coefficient of Ruby . . . . . 10

2.2.2 PS Coefficient of Polycrystalline Alumina . . . . . 12

2.2.3 PS Coefficient of Alumina Fibers in Tension . . . . . 12

2.2.4 PS Coefficient of Alumina Nanocomposites in Compression . . . . 13

2.3 Deconvolution and Curve-fitting of Photo-luminescent Data . . . . . 15

CHAPTER 3 MANUFACTURING AND MATERIAL PROPERTY DETERMINATION OF ALUMINA NANOCOMPOSITES . . . . . 17

3.1 Manufacturing of Bulk Composite Specimens . . . . . 17

3.2 Density Measurements for Volume Fraction Verification . . . . . 19

3.3 Elastic Modulus Determination . . . . . 21

3.4 Intensity Variance Determination for Dispersion Verification . . . . . 22

CHAPTER 4 CALIBRATION OF ALUMINA-EPOXY NANOCOMPOSITES USING PIEZOSPECTROSCOPY . . . . . 24

4.1 Experimental Objectives . . . . . 24

4.2 Experiment Instrumentation . . . . . 24

4.3 Data Collection Methodology . . . . . 25

4.3.1 PL Data Collection . . . . . 25

4.3.2 FBG Sensors for Strain Measurements . . . . . 28

4.4 Results of the Bulk Tensile Experiments . . . . . 29

4.5 Discussion of Bulk Tensile PS Results . . . . . 34

4.5.1 Effect of Nanoparticle Volume Fraction . . . . . 34

4.5.2 Micromechanic Effects in Tension . . . . . 36

4.5.3 R1 and R2 Peak Splitting Results . . . . . 37

4.5.4 PS Coefficient for 21.0%, 31.2%, and 34.5% Volume Fraction Nanocomposites in Tension . . . . . 40

4.5.5 Comparison With Compression Results . . . . . 42

CHAPTER 5 APPLICATION OF A CARBON-FIBER ALUMINA STRUCTURAL COMPOSITE USING PSLS . . . . . 45

5.1 Experimental Objectives . . . . . 45

5.2 Background . . . . . 45

5.2.1 Carbon Fiber-Alumina Composites . . . . . 45

5.2.2 Structural Health Monitoring Methods for Carbon Fiber Composites 46

5.2.3 Stress-Sensing Capability of Alumina Nanoparticles . . . . . 47

5.3 Manufacturing of Carbon Fiber Alumina Specimen . . . . . 48

5.4 Experimental Instrumentation . . . . . 50

5.5 Data Collection Methodology . . . . . 51

5.5.1 PL Data Collection . . . . . 51

5.5.2 DIC Strain Measurements . . . . . 52

5.6 Results and Discussion . . . . . 53

5.6.1 Particle Dispersion . . . . . 53

5.6.2 Stress-Sensing Potential . . . . . 54

CHAPTER 6 CONCLUSIONS . . . . . 57

6.1 Summary of Results . . . . . 57

LIST OF REFERENCES . . . . . 59

# LIST OF FIGURES


2.1 Spectral Emission of $\alpha$-Alumina . . . . . 8

2.2 Piezospectroscopic Effect . . . . . 9

2.3 PS Coefficients of Variable Volume Fractions in Compression [1] . . . . . 14

2.4 Experimental, Fitted, and Deconvoluted Data Comparison . . . . . 16

3.1 Manufacturing of Bulk Alumina Including, A) High-Shear Mixing B) Bulk Material in Molds and C) Curing of Bulk Material . . . . . 18

3.2 Bulk Tensile Specimen Schematic . . . . . 19

3.3 Intensity Variance for Dispersion Verification . . . . . 23

4.1 Experimental Setup . . . . . 25

4.2 Experimental Loading Scheme . . . . . 26

4.3 Snake Scan Method of 24 Point Map . . . . . 27

4.4 FBG Attachment to a Tensile Specimen . . . . . 29

4.5 21.0% R1 and R2 Peak Shift with Strain . . . . . 31

4.6 31.2% R1 and R2 Peak Shift with Strain . . . . . 32

4.7 34.5% R1 and R2 Peak Shift with Strain . . . . . 33

4.8 PS Results for Variable Volume Fractions . . . . . 35

4.9 Elastic Limit by Volume Fraction . . . . . 36

4.10 Peak Separation with Increasing Tensile Load . . . . . 38

4.11 Fracture Results . . . . . 39

4.12 PS Coefficient Range for 21.0%, 31.2%, and 34.5% Nancomposites in Tension 41

5.1 Carbon Fiber Specimen with Embedded Alumina Nanoparticles . . . . . 49

5.2 Carbon Fiber Experimental Setup . . . . . 50

5.3 Snake Scan Method of 36 Point Map . . . . . 51

5.4 DIC Speckles on the Carbon Fiber Alumina Specimen . . . . . 52

5.5 Embedded Alumina PL Intensity Results . . . . . 54

5.6 Top Row: Peak Shift with Increasing Applied Load, Bottom Row: DIC Strain Field with Increasing Applied Load . . . . . 56

# LIST OF TABLES


3.1 Alumina Nanocomposite Specimen Cross-Sectional Dimensions . . . . . 19

3.2 Measured Density of Variable Volume Fraction Specimen . . . . . 20

3.3 Theoretical Elastic Modulus . . . . . 21

3.4 Intensity Variance Data Collection Parameters and Results . . . . . 22

4.1 Data Collection Parameters . . . . . 27

4.2 PS Coefficient Range by Volume Fraction in Tension . . . . . 41

4.3 Comparison of Compression and Tensile PS Coefficient Magnitude Ranges 44

5.1 Carbon Fiber Alumina Specimen Specifications . . . . . 49

# CHAPTER 1
# INTRODUCTION

## 1.1 Motivation and Background

Composite materials offer several benefits over their metallic counterparts, in that they can be lighter, stronger, and more durable and this has increased their use in industry. Along with the increased use of these composites, the need for monitoring their structural integrity arises. In recent years, researchers have proposed the use of rigid particle additives which have positive effects on the tensile properties, fracture toughness, and energy release rate of the composite [2, 3, 4, 5]. In addition to increasing the mechanical properties, when photo-luminescent materials are used, such as ruby and alumina, optical methods can been used to non-invasively track changes in stress by monitoring spectral shifts with high spatial resolution. Upon laser excitation, the spectral response of these materials produce two characteristic peaks known as R-lines. Grabner introduced the piezospectoscopic (PS) effect, which relates the frequency shifts of these R-lines to applied stress through the PS coefficient [6]. Results from previous studies on the PS effect of polycrystalline alumina [7, 6, 8] and ruby [9, 10] were successful in characterizing the compressive stress induced shifts of the R-line peaks for polycrystalline alumina and the PS effects for ruby under uniaxial compressive stress.

Previous studies by Stevenson, successfully demonstrated that embedding nano-sized alumina particles in an epoxy matrix (nanocomposite), increased the sensitivity of the

alumina particle's response to an applied stress on the overall composite as shown by the increase in the PS coefficient determined as the peak shift response to composite stress [1]. The increase of the PS coefficient of the nanocomposites culminates to a more stress-sensitive material [1]. Furthermore, this study demonstrated that increasing the volume fraction of alumina nanoparticles in a nanocomposite increased the transferability of the applied load to the nanomodifiers [1]. The load transferred to the particles was determined to correspond to an increase in the the piezospectroscopic (PS) coefficient.

In another study by Jones, it was determined that unlike static PS coefficients which vary in sensitivity due to volume fraction, alumina nanocomposites tested under low compressive strain rates have an increased sensitivity with increasing strain rate [11]. This work successfully illustrated the capability of alumina nanoparticles as stress sensors. It was also concluded that piezospectroscopy can be used to determine early failure in nanocomposites by monitoring changes in the load transferred to the particles [11].

The experiments by Stevenson and Jones have successfully shown the ability to use alumina particles for stress-sensing in compression. However, the PS characterization of an alumina nanocomposite in tension remains to be determined. Since, nanocomposites in tension may present different characteristics than in compression, it is important to understand how the PS response will be affected by the changes in mechanical properties, distribution of the modifiers, and the micromechanics of the nanocomposite.

## 1.2 Effects of Nano-Sized Modifiers in Epoxy

Traditional polymer composites filled with micron-sized fillers often show improvements in their mechanical properties in the form of a higher modulus, higher yield strength, and higher glass transition temperature [12, 13]. It has been recently determined that the integration of nano-sized particles into a polymer matrix increases the strength of the polymer more than micron-sized particles. Nanoparticles do not impede the matrix deformation as much as micron-sized particles because they integrate better into the polymer microstructure due to the near molecular dimension of the particle [14].

The small particle size leads to smaller defects within the matrix and increases the particle to matrix interfacial area [4, 15, 16, 17]. Higher specific areas between the particles and matrix may play an important role in the toughening effect as increased interfacial area allows the epoxy to bond to more particles. The strength of the interfacial layer will be dependent on the adhesion of the individual particles to the matrix [12, 13, 18]. Limited interfacial adhesion allows for debonding and nano-void formation to occur during mechanical loading [19]. For the development of alumina stress-sensing nanocomposites, the nanoparticles must be well dispersed and have excellent adhesion to the epoxy.

The effective elastic modulus and tensile strength of the nanocomposite is also dependent on the volume fraction of the particles in the matrix [20, 21]. It has been established that the effective elastic modulus increases with the volume fraction of particles and is

also linearly dependent on the nanoparticle content [2, 14, 18, 14, 22]. Even at low particle volume fractions a significant change in material properties can exist. It has been shown that 43% volume fraction of $\alpha$-alumina is the maximum volume fraction of particles that can be added to an epoxy without degrading the mechanical properties [23]. It has been also been shown that nano-particle agglomerations are promoted as the volume fraction of particles is increased [13, 24]. Agglomerations degrade the polymers performance because these regions act as preferred sites for nucleation, crack initiation, and allow failure to occur more easily [24]. Particle agglomerations also change the effect of the sensing particles which will affect the accuracy of the particle's response to the stress applied. Agglomerations may also cause an early failure of the particle to matrix adhesion at the agglomeration site limiting the stress-sensing range of the alumina nanoparticles. As the volume fraction is increased, the surface-to-surface interparticle distance between agglomerates decreases [14]. The reduction of the interparticle distance allow for cracks to coalesce at a lower mechanical load. Therefore, volume fraction effects should be considered in the development of alumina stress-sensing material.

## 1.3 Micromechanics of Nanocomposites

Under load, material imperfections such as voids, inclusions, and defects often induce stress concentrations [24]. Even though nanoparticles cause small deviations in their local environment, these small deviations can sum up to significant contributions to the

macroscopic mechanical performance [24]. Nanoparticle modifiers in an epoxy matrix produce a much larger number of nucleating sites where micro cracks can form. But in turn, significantly reduce the size of these locations [13]. It has been proposed that nanoparticles actually promote the formation of subcritical microcracks, which delay material failure by reducing the formation of critical cracks formed by microcrack coalescence [14]. In tension, nucleating sites and voids are more readily formed because disentanglement and/or rupture of the chain molecules are favored [24]. The combination of nanovoid enlargement and the extension of the epoxy matrix strands exhibit very similar behavior to crazing in an amorphous polymer [19]. Crazing is defined as a network of fine cracks on or under the surface of a material [25].

As the volume fraction of the nanocomposite increases, the mechanism of nanoparticle induced crazing also increases [19]. Nanocomposites with high volume fractions of nanoparticles succumb to large agglomerations that tend to initiate voids and exhibit brittle behavior through rapid crack propagation [19]. Since nanoparticles promote the formation of a large number of subcritical micro cracks, the propagating crack front would interact with far more particles in the nanocomposite than in a micron-composite which causes a change in the fracture mechanics [14]. Although changes in the fracture mechanics of nanocomposites are important to understand the nanocomposite failure, debonding and plastic void growth are the key mechanisms to improved crack resistance for nanocomposites [26, 18]. Due to crazing effects, it is expected that the particles will debond from the matrix earlier than overall material failure. Through the use of

piezospectroscopy, the relief of load transfer to the particle will be corresponded with the formation of subcritical microvoids. In this study, the change in PS response of the particles due to loss in the load transferred will be correlated to a relief in the stress experienced by particles. The ability to detect the micromechanic effects using PS will demonstrate the stress-sensing capability of alumina nanoparticles.

## 1.4 Overview of Research

In this work, photo-luminescent $\alpha$-alumina nanoparticles were embedded into an epoxy matrix and monitored in-situ to determine the nanoparticle response to tensile mechanical loading. Tensile specimens of alumina-epoxy nanocomposite were fabricated using 21.0%, 31.2%, and 34.5% volume fraction of nanoparticles and loaded to failure. The spectral frequency shifts of the R-lines in relation to applied tensile stress were calibrated by means of the PS coefficient. The application of this method to a novel structural health-monitoring application will be investigated through the use of embedded alumina nanoparticles in a carbon-fiber composite.

In Chapter 2, the theory of $\alpha$-alumina photo-luminescence, method of piezospectroscopy, the development of the PS coefficient of ruby, polycrystalline alumina, alumina fibers, and alumina nanoparticles in compression will be discussed. Chapter 2 will also include a discussion of the deconvolution and curve-fitting of photo-luminescent data. Chapter 3 will discuss the manufacturing of the tensile alumina-epoxy specimens, the

density measurements for volume fraction verification, the determination of theoretical Elastic Modulus for the bulk alumina-epoxy material, and the intensity variance determination for the verification of particle dispersion. In Chapter 4, the experiment instrumentation, data collection methodology for the photo-luminescent data and strain measurement will be discussed. The results of the tensile PS calibration results of the nanocomposite will be discussed. Chapter 5 will discuss the motivation and background of the carbon fiber alumina structural composite study. The manufacturing of the carbon fiber alumina specimen along with the experimental instrumentation and data collection methodology is also discussed. Chapter 5 includes the discussion of the results from carbon fiber alumina structural composite study. Lastly, Chapter 6 will discuss the conclusions and future works of this study.

# CHAPTER 2
# PHOTO-LUMINESCENCE, PIEZOSPECTROSCOPY, AND DECONVOLUTION

## 2.1 Theory of $\alpha$-Alumina Photo-luminescence

$Cr^{3+}$ ions are naturally occurring impurities within the crystal structure of $\alpha$-alumina. Spectral emission occurs when the $Cr^{3+}$ ions transition from an excited state back to ground state upon laser excitation. The emitted photons form the characteristic R-lines which have two distinct peaks known as R1 and R2 occurring at 14403 $cm^{-1}$ and 14433 $cm^{-1}$ respectively [27], as shown in Figure 2.1.

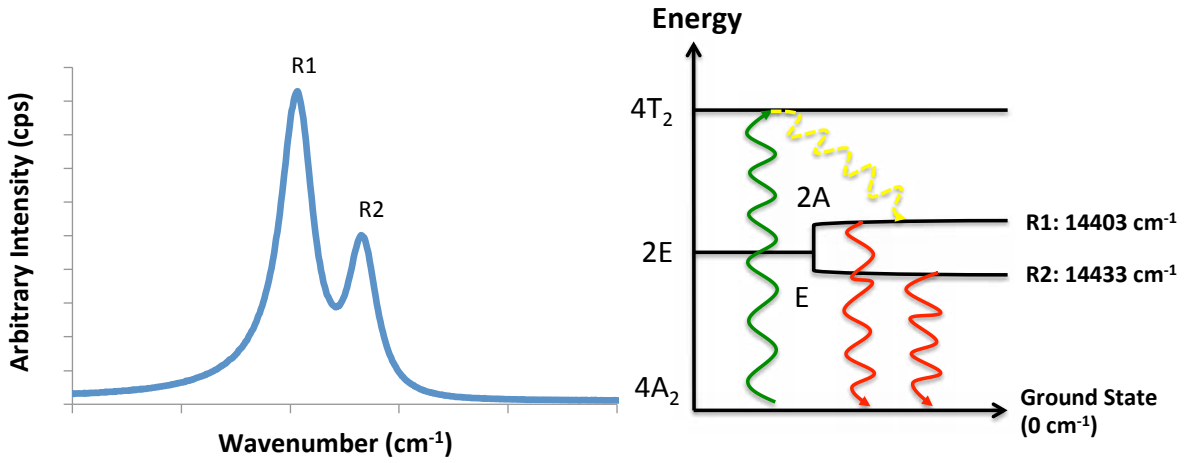


Figure 2.1: Spectral Emission of $\alpha$-Alumina

## 2.2 Piezospectroscopy

The piezospectroscopic (PS) effect as shown in Figure 2.2 relates the frequency shifts of the R-lines to stress for ruby and polycrystalline alumina. The stress sensing capabilities of $\alpha$-alumina are possible due to these frequency shifts which are caused by deformation of the crystal field surrounding the $Cr^{3+}$ ions [28, 29].

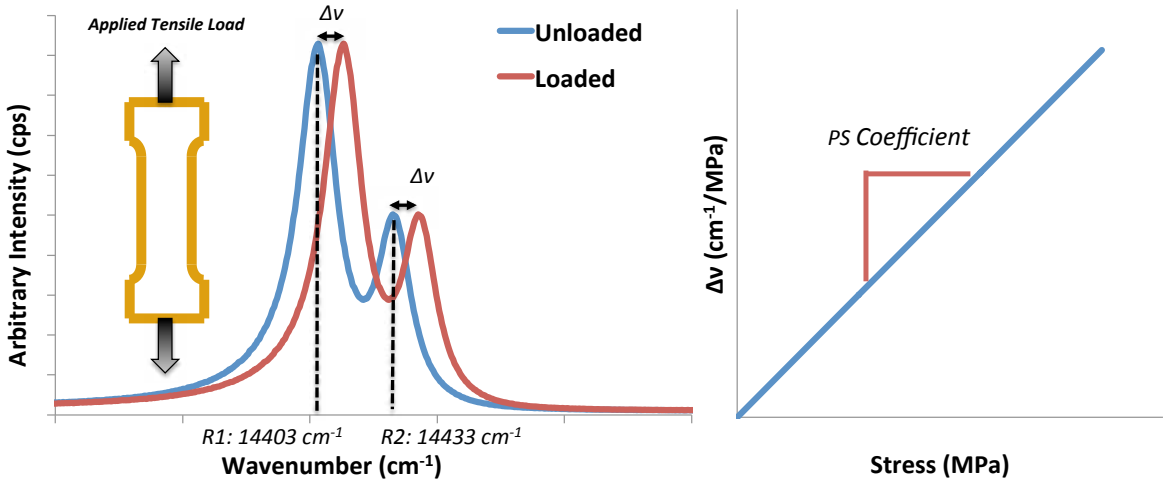


Figure 2.2: Piezospectroscopic Effect

While the calibration of the PS effect, or PS coefficient for ruby and polycrystalline alumina has been determined in tension and compression, the PS behavior of alumina nanocomposites has only recently been determined in compression [8, 1]. Several studies will be outlined in the following section to highlight the important previous relationships and reported PS coefficients.

### 2.2.1 PS Coefficient of Ruby

Ruby, also known as $Cr^{3+}$-doped sapphire crystal, has been extensively studied using photo-stimulated luminescent spectroscopy (PSLS). During the early years of single crystal ruby luminescence studies, one major success was the observation that a frequency shift of the characteristic R1 and R2 peaks occurs when uniaxial stress was applied [9]. Kaplyanskii [30] introduced the first model of the PS effect using the following equation:

$$\Delta\nu = A\left(\sigma_1 + \sigma_2\right) + B\sigma_3 \tag{2.1}$$

where $\Delta\nu$ represents the frequency shifts, $\sigma_1$, $\sigma_2$, and $\sigma_3$ are the normal stress directed along the crystallographic axes, and $A$ and $B$ are the PS coefficients. This equation relates the frequency shifts of the R-lines as a linear function of stress. Later, peaks within the vibronic sidebands of the ruby emission spectrum were also determined to exhibit stress-sensitive behavior which could potentially be used in the piezospectroscopic model [10].

Forman [31] first applied the use of spectral shifts of ruby R-lines to measure the hydrostatic stress in diamond anvil cells and developed the following equation to relate the frequency shifts of the R-lines to hydrostatic stress:

$$\Delta\nu = \pi_H\sigma_H \tag{2.2}$$

where $\Delta\nu$ is the frequency shift, $\sigma_H$ is the hydrostatic stress, and $\pi_H$ is the PS coefficient. The PS coefficient of ruby under hydrostatic stress was determined to be 7.59 $cm^{-1}/GPa$ for R1 and 7.615 $cm^{-1}/GPa$ for R2.

Using Forman's relationship between frequency shifts and hydrostatic stress, Grabner [6] introduced the following tensorial equation to relate the frequency shifts of the R-lines to stress:

$$\Delta\nu = \pi_{ij}\sigma_{ij} \tag{2.3}$$

where $\Delta\nu$ is the frequency shift, $\pi_{ij}$ is the PS coefficient tensor, and $\sigma_{ij}$ is the stress state as defined by the crystallographic frame of reference. Furthermore, Grabner proposed that the PS coefficient tensor, $\pi_{ij}$, is symmetric and therefore allows the effect of shear stress in ruby to be neglected in most practical situations.

He and Clarke [32] determined that point symmetry cannot be assumed because the PS response of $Cr^{3+}$ ions in sapphire is anisotropic in the basal plane. The previous tensorial equation was updated to include a coordinate transformation to a global coordinate system [8, 33]:

$$\Delta\upsilon = \pi_{ij}a_{ik}a_{jl}\sigma_{kl} \tag{2.4}$$

where $\pi_{ij}$ represents the PS coefficient, $a_{ij}$ is the transformation matrix, and $\sigma_{kl}$ is the stress state. The PS coefficients relating the frequency shifts to stress with respect to the three crystallographic directions for ruby were determined through uniaxial compression studies:

$$\Delta\nu\,(R_1) = 2.56\sigma_{11} + 3.50\sigma_{22} + 1.53\sigma_{33} \tag{2.5}$$

$$\Delta\nu\,(R_2) = 2.65\sigma_{11} + 2.80\sigma_{22} + 2.16\sigma_{33} \tag{2.6}$$

### 2.2.2 PS Coefficient of Polycrystalline Alumina

The following equation shows, the relationship that Ma and Clarke derived for the frequency shift in spectral emission from a large number of randomly oriented grains in a polycrystalline material [8]:

$$\overline{\Delta\upsilon} = \frac{1}{3}(\pi_{11} + \pi_{22} + \pi_{33})(\sigma_{11} + \sigma_{22} + \sigma_{33}) \tag{2.7}$$

By neglecting transverse stress ($\sigma_{33} = 0$) and assuming equal plane stress ($\sigma_{11} = \sigma_{22} = \sigma$), the above equation can be expressed as follows:

$$\overline{\Delta\upsilon} = \frac{2}{3}(\pi_{11} + \pi_{22} + \pi_{33})\sigma \tag{2.8}$$

By using polished polycrystalline alumina bars in a four point bending test, Ma and Clarke determined that the PS coefficient of polycrystalline alumina is 2.46 $cm^{-1}/GPa$ for R1 and 2.50 $cm^{-1}/GPa$ for R2 in tension and compression [8] .

### 2.2.3 PS Coefficient of Alumina Fibers in Tension

The PS calibration of transparent alumina fibers with an $\alpha$-alumina crystal structure (85% alumina and 15% mullite) were mounted on plastic beams and tested using the cantilever beam technique [5]. Knowing the maximum deflection of the beam, the strain

distribution of the beam, and subsequently the strain distribution of the fiber, was determined using the following:

$$\epsilon(x) = \frac{3t\delta_{max}}{2L^2}(1 - \frac{x}{L}) \tag{2.9}$$

where $t$ is the beam thickness and L is the distance between the free and fixed end of the beam. Dassios [5] determined the PS coefficient of alumina fibers to be 7.99 $cm^{-1}$ per strain (%) for R1 and 7.57 $cm^{-1}$ per strain (%) for R2 or 3.07 $cm^{-1}/GPa$ for R1 and 2.91 $cm^{-1}/GPa$ for R2 in compression and tension.

### 2.2.4 PS Coefficient of Alumina Nanocomposites in Compression

To increase the sensitivity of the PS coefficient for polycrystalline alumina, alumina nanoparticles have been embedded into an epoxy matrix in previous studies [1, 11]. Assuming that alumina nanoparticles in an epoxy matrix are experiencing hydrostatic stress, based on their size, the frequency shifts of the R-lines can be directly related to applied stress through the PS coefficient as shown in the following equation:

$$\Delta\nu = \pi_{NC}\sigma_{applied} \tag{2.10}$$

where $\Delta\nu$ is the frequency shift of the R-lines, $\pi_{NC}$ is the PS coefficient of the nanocomposite, and $\sigma_{applied}$ is the applied stress to the nanocomposite. Previous work using PSLS on alumina nanocomposites have shown a direct linear relationship between the frequency shifts of the R-lines with statically applied compressive stress as shown in

Figure 2.3. Stevenson determined that the static PS coefficient of 5%, 25%, and 38% volume fraction alumina nanocomposites are 3.16, 3.65. and 5.63 $cm^{-1}/GPa$ for R1 and 2.6, 3.42, 5.08 $cm^{-1}/GPa$ for R2 in compression [1]. The PS coefficient of the nanocomposites were observed to increase as the volume fraction of alumina nanoparticles in the epoxy increased.

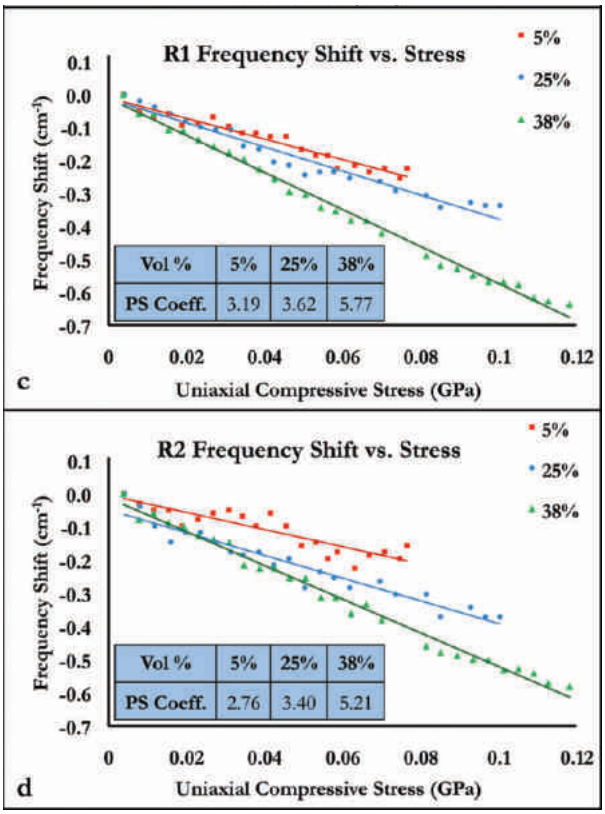


Figure 2.3: PS Coefficients of Variable Volume Fractions in Compression [1]

The increase in PS coefficient indicates increased particle sensitivity to load transfer with increasing volume fraction. Furthermore, the intensity of the photo-luminescent

response of the particles was used to verify the dispersion of the particles within the matrix and identify potential voids [1]. A study by Jones [11] on the PS effect of alumina nanocomposites under quasi-static compressive loading showed that increasing the strain rate increases the particle sensitivity for the same volume fraction and increases the PS coefficient compared to static results. The quasi-static PS coefficient range for 4.5%, 13.6%, and 29.7% are 3.34 - 4.87, 4.30 - 4.41, and 3.15 - 5.37 $cm^{-1}/GPa$ for R1 and 2.74 - 4.85, 4.06 - 4.72, and 2.62 - 5.39 $cm^{-1}/GPa$ for R2 in compression. This model for the PS effect of alumina nanocomposites has been successful in compressive studies and will also be used to determine the PS coefficient of alumina nanocomposites in tension. By using this relationship, the load transfer to the particles can be characterized.

### 2.3 Deconvolution and Curve-fitting of Photo-luminescent Data

The characteristic alumina R-lines are two distinct peaks that each share a region of data that contribute to peak positions affected by convolution in the raw experimental data shown in Figure 2.4. Due to this convolution, the raw experimental data must be fitted and deconvoluted to determine accurate peak positions and therefore obtain accurate peak position shifts. A genetic algorithm (GA) based procedure [34] has been successfully used to deconvolute R-lines peaks obtained from ruby, alumina nanocomposites embedded in an epoxy matrix [1, 11], and plasma-sprayed alumina coatings [35].

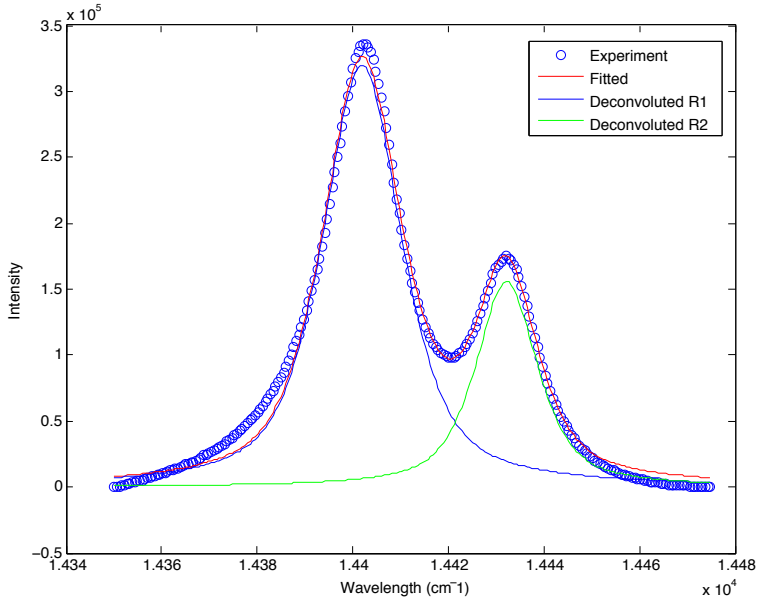


Figure 2.4: Experimental, Fitted, and Deconvoluted Data Comparison

Genetic algorithm based procedures have the capability of global optimization [36, 37]. The code used in this study uses the GA procedure while performing four main functions on unprocessed data. Specifically, these four functions are curve sectioning, baseline removal, curve separation, and curve recombination. The optimization uses two pseudo-Voigt functions [38, 39, 40] which obtain several parameters for R1 and R2, specifically, peak position, peak intensity, area, curve width, and goodness of fit. After raw data has been processed, the true peak positions are realized and peak shifts can be accurately calculated. Piezospectroscopy can then be utilized to determine the micro-scale load transfer through the PS coefficient as described in the previous sections.

# CHAPTER 3
# MANUFACTURING AND MATERIAL PROPERTY DETERMINATION OF ALUMINA NANOCOMPOSITES

## 3.1 Manufacturing of Bulk Composite Specimens

The bulk alumina-epoxy composite was fabricated using a procedure similar to previous studies [1]. The $\alpha$-alumina nanopowder had an average particle size of 150 nm, 99.85% purity, and a density of 3.97 $g/cm^3$. The epoxy resin was Epon 862 (Bisphenol-F type) which has a density of 1.17 $g/cm^3$ and the curing agent was Epikure-W. Volume fractions were chosen to correspond with previous work [1, 11] and resulted in 21.0%, 31.2%, and 34.5% alumina nanoparticles. Figure 3.1 shows the manufacturing process that was followed to create the bulk composite material. The epoxy and particles were mixed together using a high shear mixer for 1 hour. The use of a high shear mixture allows for a well blended composite and promotes the removal of most agglomerates that may have been present. The curing agent was measured and added to the particle-epoxy mixture and mixed for an additional hour. A low-pressure vacuum system was then used for approximately 1 hour to remove most of the air bubbles that may have been introduced during the mixing. The material was poured into a mold and cured for 4 hours in a furnace at 120 °C. After the curing process was complete, the mold was removed from the furnace, and the bulk nanocomposite was removed while the mold was still warm using a gentle extraction process. The tensile dogbone specimens were cut as shown in Figure 3.2 using a water-jet cutting method. Aluminum end tabs were added to the ends

of each specimen in order to allow the wedge grips to adequately hold the specimen to prevent each specimen from slipping prematurely and cracking under the force of the grips. Table 3.1 shows the dimensions of each bulk tensile specimen.

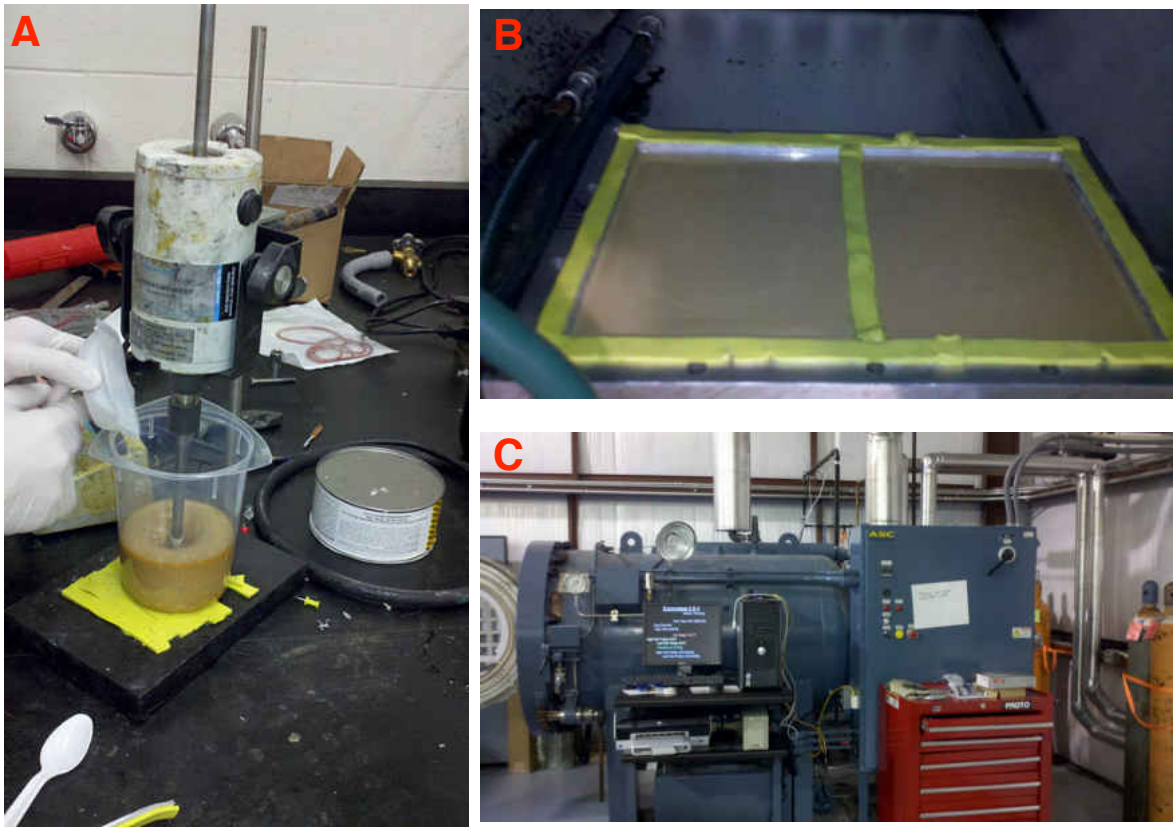


Figure 3.1: Manufacturing of Bulk Alumina Including, A) High-Shear Mixing B) Bulk Material in Molds and C) Curing of Bulk Material

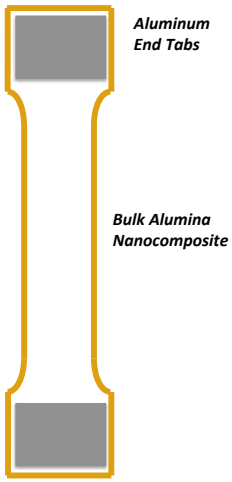


Figure 3.2: Bulk Tensile Specimen Schematic

Table 3.1: Alumina Nanocomposite Specimen Cross-Sectional Dimensions

| Volume Fraction % | Width (mm) | Thickness (mm) | Cross-Sectional Area ($mm^2$) |
|---|---|---|---|
| 21.0 | 9.0 | 7.5 | 67.5 |
| 31.2 | 10.1 | 8 | 84.0 |
| 34.5 | 8.0 | 7.0 | 56.0 |

## 3.2 Density Measurements for Volume Fraction Verification

The actual volume fraction of each manufactured sample was determined by measuring the density of the nanocomposite. Using the following equations, the actual volume

fraction of alumina nanoparticles for each specimen was calculated:

$$\rho_{NC} = v_f \rho_f + v_m \rho_m \tag{3.1}$$

$$v_m = 1 - v_f \tag{3.2}$$

where $\rho_{NC}$ is the measured density of the nanocomposite, $v_f$ is the volume fraction of filler, $v_m$ is the volume fraction of the matrix, and $\rho$ is the known density for the filler and matrix. Table 3.2 shows the measured density of each nanocomposite and the resultant volume fraction of the filler and matrix material.

Table 3.2: Measured Density of Variable Volume Fraction Specimen

| Volume Percent of Filler | Volume Percent of Matrix | Density (g/cm$^3$) |
|---|---|---|
| 21.0 | 79.0 | 1.76 |
| 31.2 | 68.8 | 2.05 |
| 34.5 | 65.5 | 2.14 |

The results shown in Table 3.2 demonstrate an increase in the measured densities of 1.76, 2.05, and 2.14 $g/cm^3$. These results correspond to an increase in the volume fraction of alumina nanoparticles in the nanocomposite. Also shown in Table 3.2 is the resultant volume fraction for each specimen which were determined to be 21.0%, 31.2%, and 34.5% volume fraction of alumina nanoparticles. Since the addition of fillers has been determined to change the mechanical properties of polymer [2, 14, 18, 14, 22], the

response to mechanical loading for nanocomposite of lower volume fraction is expected to be dominated by the matrix behavior while the response of higher volume fraction nanocomposites is expected to be dominated by the rigidity of the ceramic modifiers.

### 3.3 Elastic Modulus Determination

Using the theory of the rule of mixtures, the theoretical elastic modulus for the nanocomposites, $E_{NC}$ can be determined by using the following equation:

$$E_{NC} = v_f E_f + v_m E_m \tag{3.3}$$

where $v_f$ is the filler volume fraction, $E_f$ is the elastic modulus of the filler, $v_m$ is the matrix volume fraction, and $E_m$ is the elastic modulus of the matrix. As shown in Table 3.3, the theoretical elastic modulus for 21.0%, 31.2%, and 34.5% volume fraction nanocomposites was determined to be 64.2, 94.6, and 104.5 $GPa$, respectively.

Table 3.3: Theoretical Elastic Modulus

| Volume Percent of Filler | Volume Percent of Matrix | Theoretical $E_{NC}(GPa)$ |
|---|---|---|
| 21.0 | 79.0 | 64.2 |
| 31.2 | 68.8 | 94.6 |
| 34.5 | 65.5 | 104.5 |

### 3.4 Intensity Variance Determination for Dispersion Verification

Previous work by Stevenson [1] verified the ability to determine alumina-epoxy composite sample dispersion using the PSLS method. Using a spectrometer and coupled fiber optic probe, intensity measurements for each specimen were collected. Table 3.4 shows the exposure time, the number of accumulations, the maximum obtained intensity of R1, and the minimum obtained intensity of R1. A 24 point map was collected for each sample from an area measuring 6mm X 4mm in the center of each specimen.

Table 3.4: Intensity Variance Data Collection Parameters and Results

| Volume Fraction (%) | 21.0 | 31.2 | 34.5 |
|---|---|---|---|
| Exposure Time (sec) | 0.05 | 0.01 | 0.01* |
| Number of Accumulations | 3 | 3 | 3 |
| Maximum R1 Intensity (cps) | 784 E+03 | 459 E+03 | 339 E+03 |
| Minimum R1 Intensity (cps) | 697 E+03 | 412 E+03 | 281 E+03 |

*Reduced CCD Area

Each data point was deconvoluted using the procedure described in Chapter 2. The maximum and minimum intensity value for each specimen's 24 point map were compared and dispersion was characterized as the variance of intensity using equation 3.4:

$$Intensity\,Variance\,\% = \left(\frac{Maximum\,Intensity - Minimum\,Intensity}{Maximum\,Intensity}\right) * 100 \quad (3.4)$$

The result for each sample is presented in Figure 3.3. Of the three volume fractions investigated, the 34.5% volume fraction had the highest intensity variance of 17% where the 31.2% and 21.0% volume fractions resulted in similar variances of 10% and 11% respectively. Therefore, it can be concluded that more well dispersed alumina nanoparticles occurred in volume fractions up to 31.2% and further increase in the volume fraction of alumina nanoparticles caused more significant variations. As expected higher volume fractions show the poorest dispersion. Since the load transfer to the particles may be affected by agglomerations and voids, these dispersion results can be used to improve the manufacturing process.

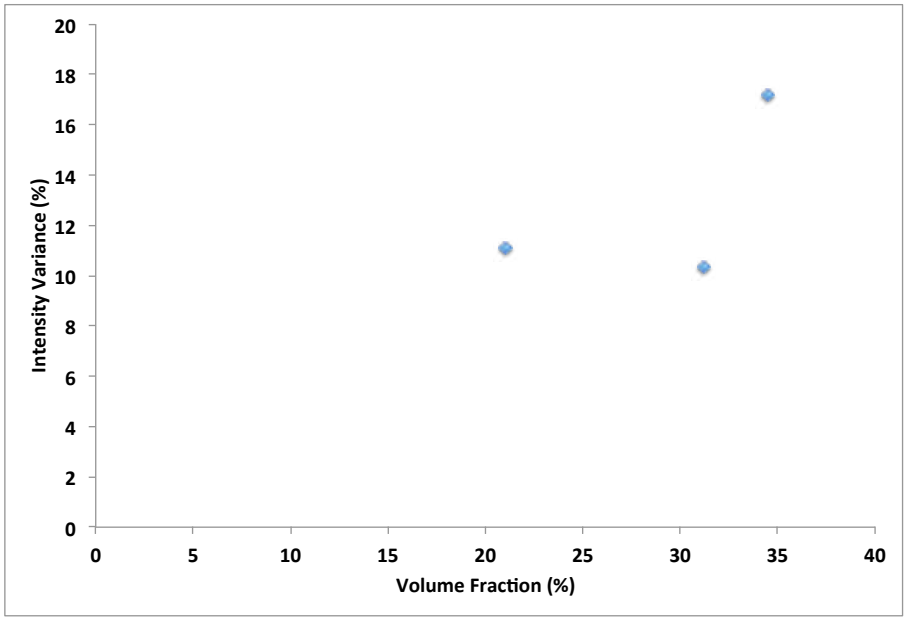


Figure 3.3: Intensity Variance for Dispersion Verification

# CHAPTER 4
# CALIBRATION OF ALUMINA-EPOXY NANOCOMPOSITES USING PIEZOSPECTROSCOPY

## 4.1 Experimental Objectives

In this study, photo-luminescent $\alpha$-alumina nanoparticles were embedded into an epoxy matrix at 21.0%, 31.2%, and 34.5% volume fraction of alumina nanoparticles and manufactured into dogbone shaped specimens. To elucidate the contribution of micromechanics to the overall behavior of the nanocomposite, the high-spatial resolution capability of the PS method was used to sense changes in the load transfer to the particles in the nanocomposite, by monitoring the stress induced shifts in the characteristic R-lines. The calibration of this material was determined as the PS coefficient for each volume fraction.

## 4.2 Experiment Instrumentation

For the collection of the PSLS data, a Renishaw Raman spectrometer with a 2400 $l/mm$ grating and attached fiber optic probe was used and calibrated using a Ne-Ar source. An argon laser of 532 $nm$ wavelength and approximately 17 $mW$ of power at the exit of the probe was used to excite the alumina particles. The probe was attached to an XYZ stage to allow for the collection of spectral maps. A MTS Insight Electromechanical system with a calibrated 10 $kN$ load cell and wedge grips were used to apply a tensile load

by deflecting the crosshead incrementally. Figure 4.1 shows the complete experimental setup.

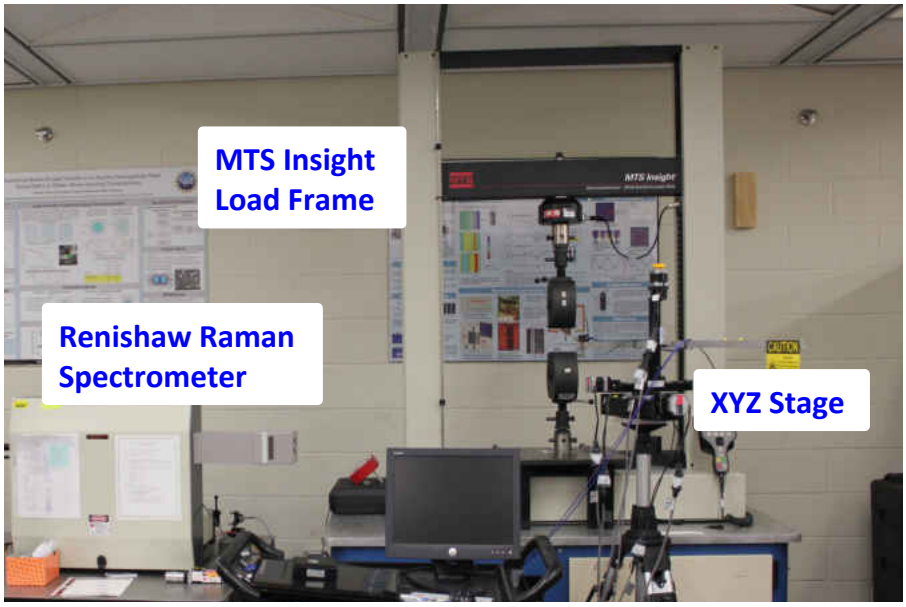


Figure 4.1: Experimental Setup

## 4.3 Data Collection Methodology

### 4.3.1 PL Data Collection

The specimen was subjected to incremental tensile loads which were held at prescribed static values for 3 minutes to allow for PL data collection as shown in Figure 4.2. The 21.0% and 31.2% volume fractions were loaded in tension up to failure. The 34.5% volume fraction was loaded up to 0.05 strain %.

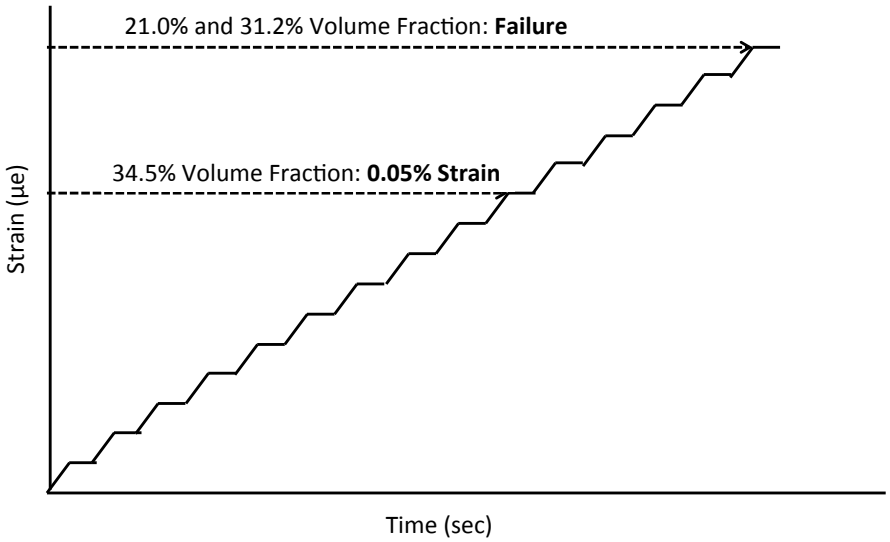


Figure 4.2: Experimental Loading Scheme

At each static hold, a spectral map of 24 points covering an area of 6mm X 4mm in the gage section of the dogbone specimen was collected by using a snake scan method as shown in Figure 4.3. The exposure time and number of accumulation for each specimen are shown in Table 4.1.

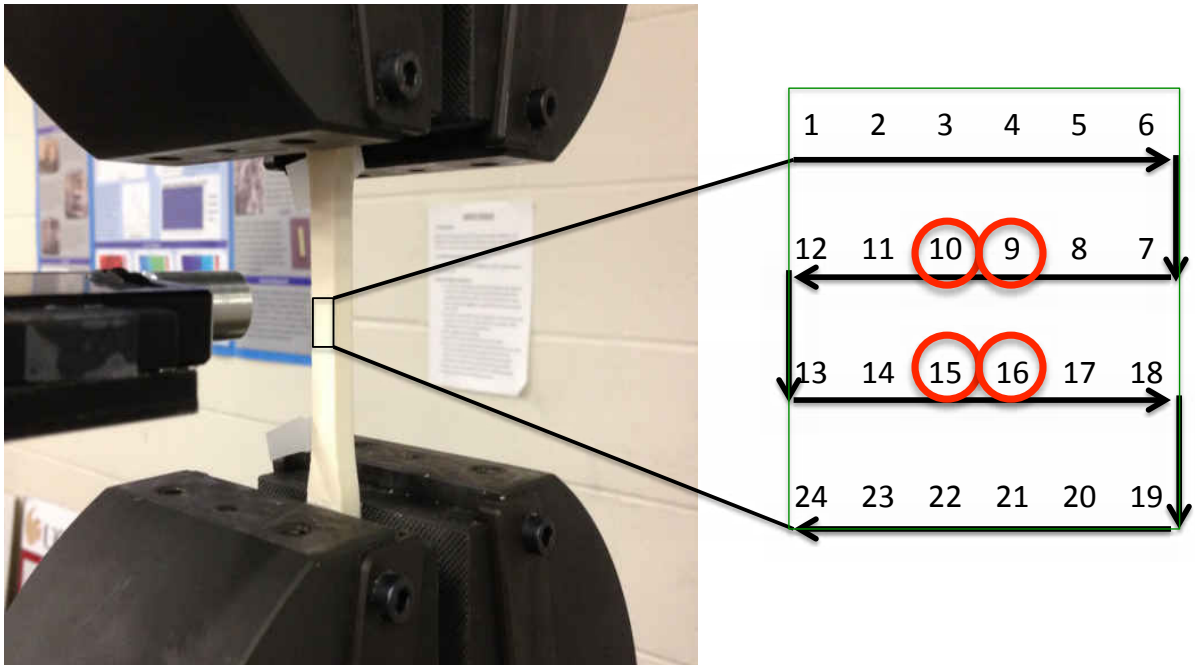


Figure 4.3: Snake Scan Method of 24 Point Map

Table 4.1: Data Collection Parameters

| Volume Fraction (%) | Exposure Time (sec) | Number of Accumulations |
|---|---|---|
| 21.0 | 0.05 | 3 |
| 31.2 | 0.01 | 3 |
| 34.5 | 0.01* | 3 |

*Reduced CCD Area

Along with collecting photo-luminescent data for each sample, strain data was collected from a Fiber Bragg Grating (FBG) sensor to measure the macro-level strain of the nanocomposite.

### 4.3.2 FBG Sensors for Strain Measurements

FBG sensors are permanent and periodic perturbations in the index of refraction of the optical fiber core [41]. The grating functions like a filter in that it reflects back a specific wavelength, which depends on the spacing of the grating, while allowing all other wavelengths to transmit [41]. As the material to which the grating is attached is affected by compressive or tensile displacement, the spacing of the grating changes, which causes a shift in the filtered wavelength [41]. The shift in Bragg wavelength with strain at a constant temperature is determined using the following equation [41]:

$$\Delta\lambda_B = 2n\Lambda\left(1 - \left(\frac{n^2}{2}\left[P_{12} - \nu\left(P_{11} + P_{12}\right)\right]\right)\right)\varepsilon \tag{4.1}$$

where $n$ is the effective index of the core, $\Lambda$ is the grating pitch, $P_{i,j}$ coefficients are the piezo coefficients of the stress-optic tensor, $\nu$ is Poisson's ratio, and $\varepsilon$ is the applied strain. In this study, the PS data will be shown with respect to the measured strain from the FBG sensor. Figure 4.4 shows the FBG sensor attached to the back side of a tensile specimen.

Figure 4.4: FBG Attachment to a Tensile Specimen

To characterize the linear PS effect of a nanocomposite as it relates to stress, the stress was approximated by Hooke's Law using the measured FBG strain:

$$\sigma_{NC} = E_{NC}\varepsilon_{FBG} \tag{4.2}$$

where $\sigma_{NC}$ is the calculated stress in the specimen gage section, $\varepsilon_{FBG}$ is the measured FBG strain, and $E_{NC}$ is the theoretical elastic modulus of the nanocomposite.

## 4.4 Results of the Bulk Tensile Experiments

The PL data for each 24 point map was post processed using the deconvolution method discussed in Chapter 2. The zero-load R1 and R2 peak positions were used as the reference positions from which successive peak shifts were measured. To reduce the influence of edge effects, four points in the center of the 24 point map were averaged

to the determine the spectral shifts for each static hold. Results will be presented with respect to microstrain, which indicates a strain of $10^{-6}$. Figure 4.5 shows the peak shift due to increasing strain for R1 and R2 for 21.0% volume fraction nanocomposite. Figure 4.6 shows the peak shift due to increasing strain for R1 and R2 for 31.2% volume fraction nanocomposite. Figure 4.7 show the peak shift due to increasing strain for R1 and R2 for 34.5% volume fraction nanocomposite.

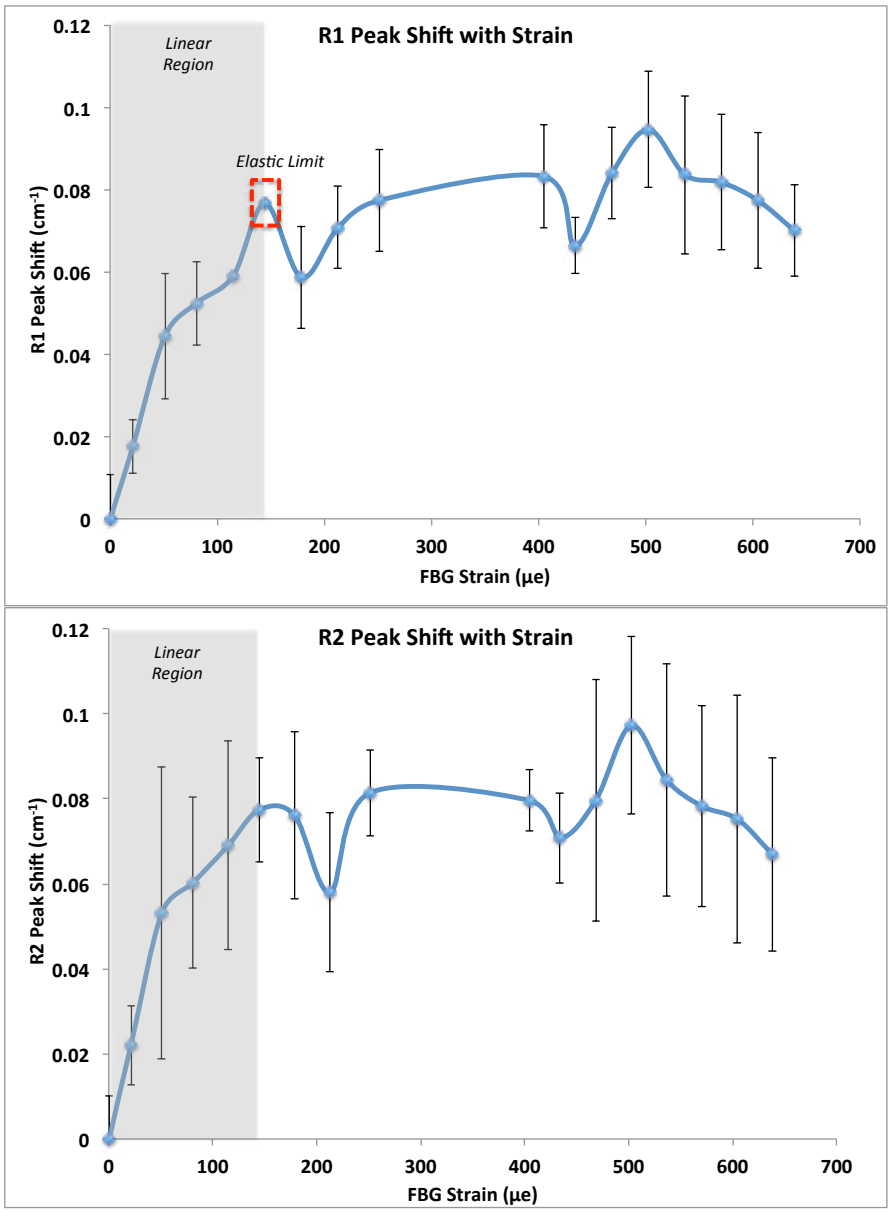


Figure 4.5: 21.0% R1 and R2 Peak Shift with Strain

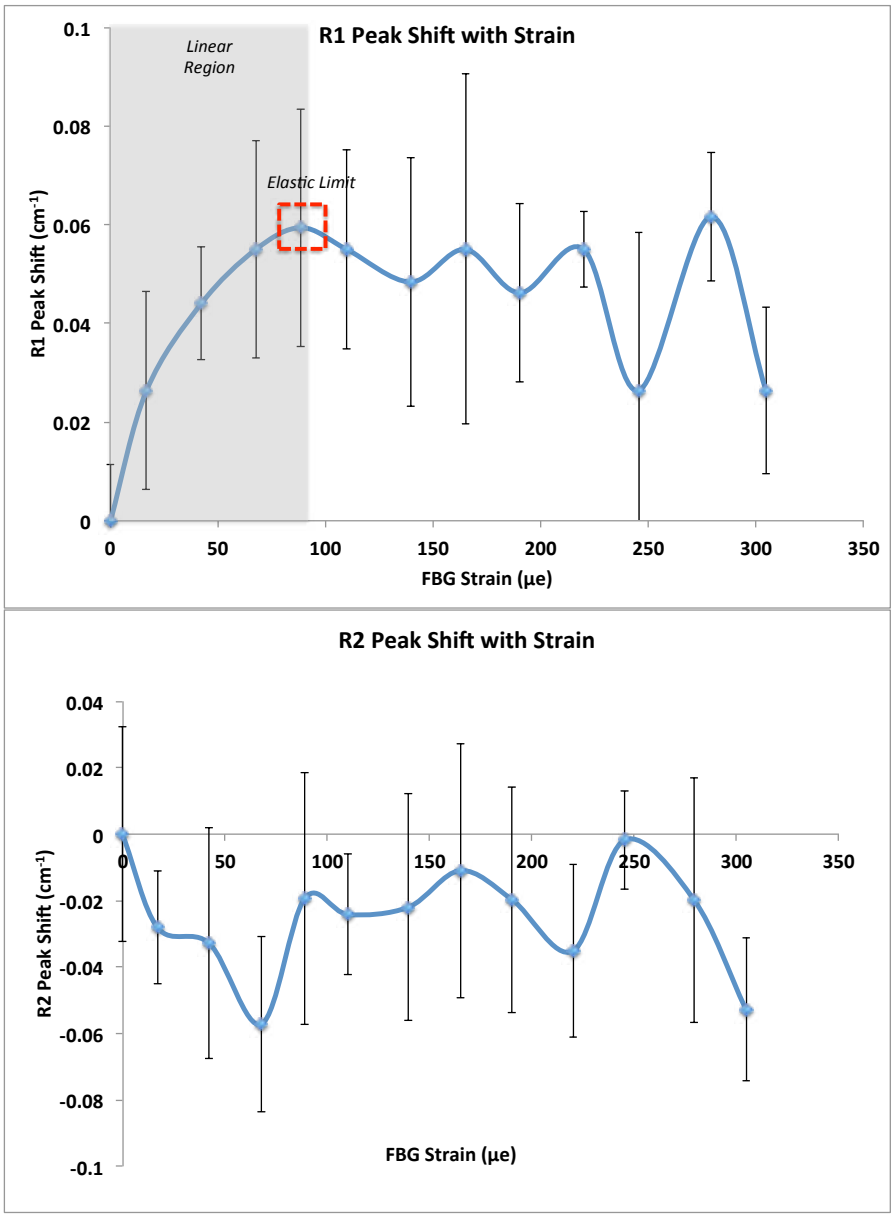


Figure 4.6: 31.2% R1 and R2 Peak Shift with Strain

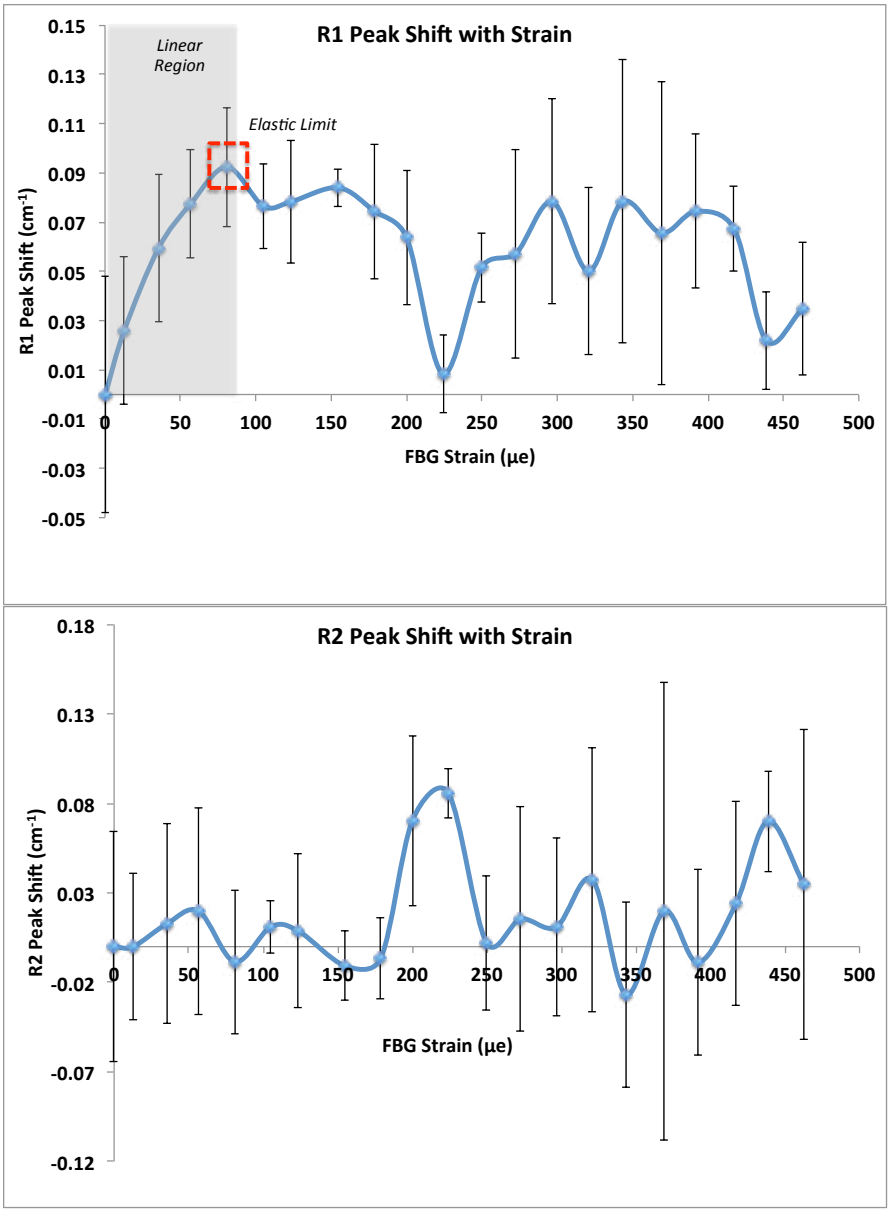


Figure 4.7: 34.5% R1 and R2 Peak Shift with Strain

Figure 4.5, 4.6, and 4.7 show that all volume fractions tested resulted in the R1 PS data showing a region of linear behavior followed by a region of non-linear behavior.

Figure 4.5, 4.6, and 4.7 show that within the R1 linear region for all volume fractions, the embedded particles exhibited positive peak shifts with increasing strain due to the applied tensile load. The end of the linear region was defined as the elastic limit or the first instance where the peak shifts change from an upward shift to a downward shift and no clear trend for the peak shift follows. The elastic limit is labeled in Figures 4.5, 4.6, 4.7. Figure 4.5 shows that the R2 peak shifts for the 21.0% volume fraction follow a similar trend as the R1 peak shifts. In the case of the 31.2% and 34.5%, the R2 peak shifts did not follow a similar trend to their corresponding R1 shifts. A detailed discussion on the volume fraction effects, differences in the R1 and R2 peaks shift trends, the observed elastic limit, and the role of micromechanic effects on these parameters is presented in the following section.

## 4.5 Discussion of Bulk Tensile PS Results

### 4.5.1 Effect of Nanoparticle Volume Fraction

Figure 4.8 compares the approximate linear region of the PS results for R1 for each volume fraction. First, it can be observed that the particle's spectral peaks shifts with increasing strain show varying relationships for each volume fraction. Figure 4.8 also shows that increasing the volume fraction increases the nanoparticle sensitivity to increasing strain as shown by the slope of the R1 peak shift versus strain relationship.

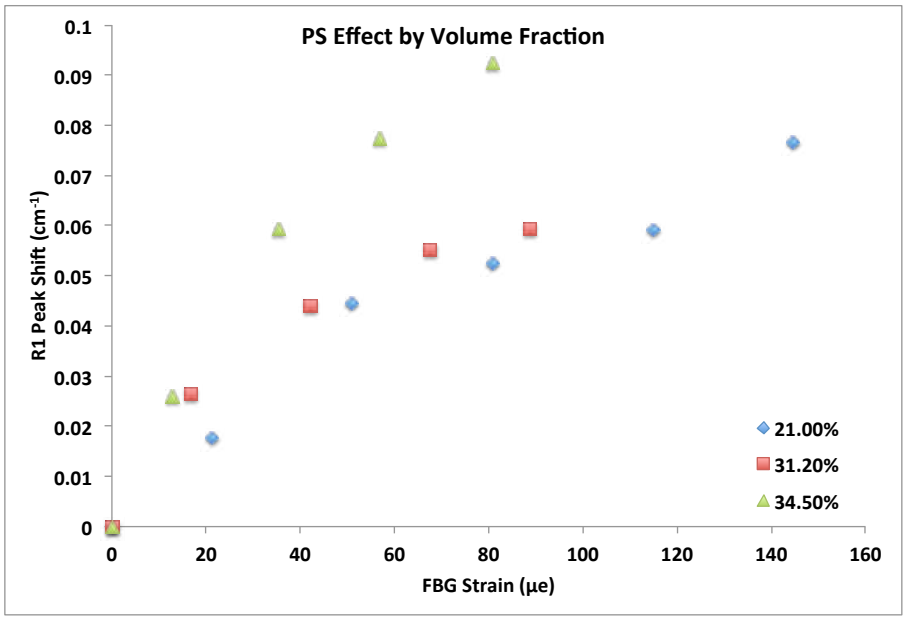


Figure 4.8: PS Results for Variable Volume Fractions

Since peak shifts of the alumina nanoparticles are directly related to the stress experienced by the nanoparticles, nanoparticles exhibiting greater R-line peak shifts are thus experiencing higher stress. This would indicate that for the same applied strain, the alumina nanoparticles in the 34.5% volume fraction specimen experienced greater stress than the alumina nanoparticles in the 21.0% and 31.2% volume fraction specimen. Since the alumina nanoparticles have a higher modulus as compared to the epoxy, it can be said that the particles are able to support more of the applied load. Therefore, an increase in the volume fraction of alumina nanoparticles improves the load transfer to the particles.

### 4.5.2 Micromechanic Effects in Tension

The PS method allows for the monitoring of the nanoparticle's behavior, the micro-scale behavior, in comparison to traditional techniques which monitor the macro scale specimen behavior. In Figures 4.5, 4.6, and 4.7 an approximate elastic limit was defined for each volume fraction. These elastic limits, as shown in Figure 4.9, were identified as the first instance where the peak shifts change from an upward shift to a downward shift.

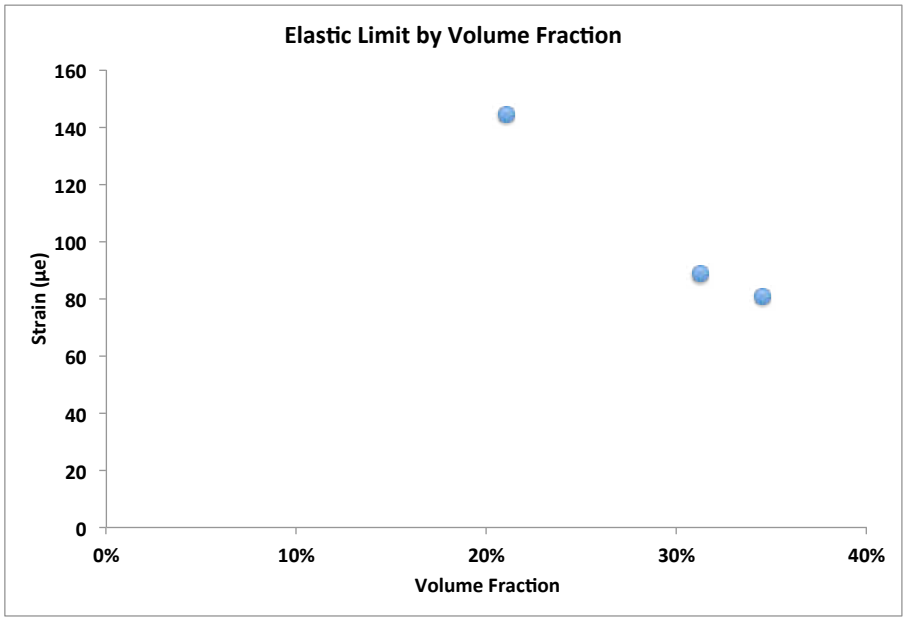


Figure 4.9: Elastic Limit by Volume Fraction

As previously discussed, the response of the alumina nanoparticles to increasing strain is due to the load transferred to the particles. At the elastic limit, it can be said that the particles begin to experience a relief in the load transfer. This relief in the load transferred

can be potentially attributed to several micromechanic factors such as interfacial layer failure, microvoid formation, and crack initiation. These micromechanic influences and the permanent damage that may be caused to the nanocomposite contribute to the non-linear response of the PS effect. In tension, it is also known that low volume fractions of filler allow for the polymer strands of the epoxy to deform in a homogeneous ductile manner. Since the majority of the nanocomposites deformation is due to the epoxy [42] and at low volume fractions the mechanical behavior of the nanocomposites is dominated by the epoxy matrix, then this explains why the 21.0% volume fraction would exhibit a higher strain at the elastic limit when compared to the the 31.2% and 34.5% volume fraction results.

### 4.5.3 R1 and R2 Peak Splitting Results

Under hydrostatic stress, the magnitude of the trigonal strain is extremely small and therefore can be neglected. In stress states that have deviated from hydrostatic stress, the trigonal strain contribution has been shown through R1 and R2 separation [43]. For ruby, Shen and Gupta determined that in tension the difference in peak position between R1 and R2 $\Delta(R1 - R2)$ increases [43]. Therefore, when peak separation is occurring, a deviation from a hydrostatic stress state has occurred [43]. For the 21.0% specimen the $\Delta(R1-R2)$ as shown in Figure 4.10 shows that $\Delta(R1-R2)$ remained relatively constant with increasing strain.

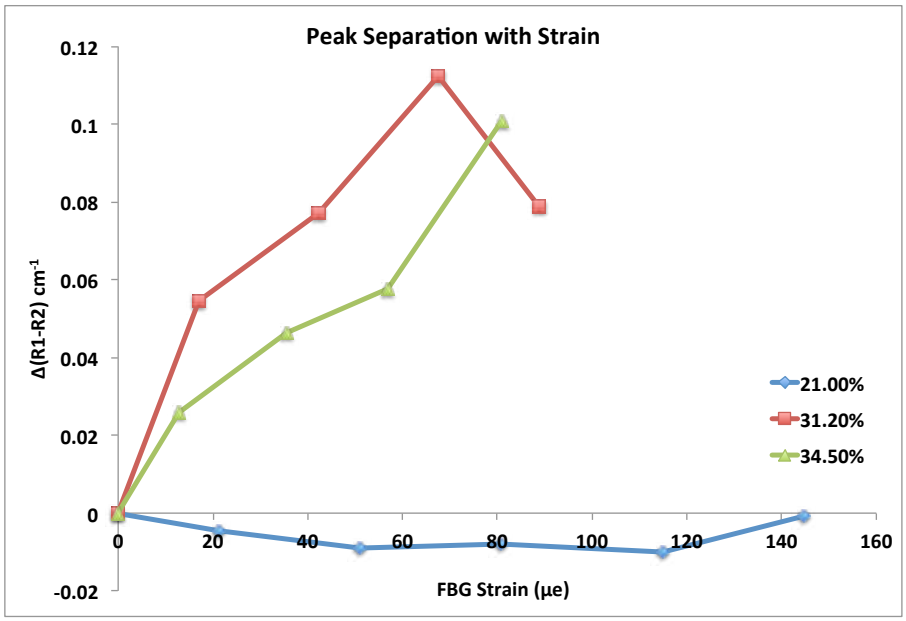


Figure 4.10: Peak Separation with Increasing Tensile Load

This response indicates that the particles in the 21.0% volume fraction specimen were experiencing hydrostatic stress as originally assumed. In the case of the 31.2% and 34.5% volume fraction an increasing trend in the $\Delta(R1 - R2)$ is noted. These results indicate a deviation from hydrostatic stress. For further verification, the fracture locations of the specimen were noted as shown in Figure 4.11 for the 21.0% and 31.2% volume fraction specimens.


Figure 4.11: Fracture Results

Since dogbone specimens are designed to fail in the gage section due to uniaxial tension, failure in another area of the specimen may be attributed to non-uniform, non-uniaxial tensile loading of the specimen. The 21.0% specimen failed in the middle of the gage section, and therefore it can be concluded that the specimen was loaded in uniform uniaxial tension. When the failure location and a relatively constant $\Delta(R1 - R2)$ are correlated together, for the 21.0% volume fraction specimen it can be concluded that the nanoparticles experienced hydrostatic stress. The 31.2% volume fraction specimen did not fail in the middle of the gage section, instead it failed closer to the grips. In this case, it can be concluded that the specimen may not have been subjected to uniaxial tensile

loads, or may have failed this way due to manufacturing issues. Both the $\Delta(R1 - R2)$ splitting and non-ideal fracture location support the deviation from hydrostatic stress for the 31.2% volume fraction specimen. The inherent challenges with manufacturing alumina nanocomposites such as particle settling which can cause slight differences in the material properties on different sides of the specimens, cutting method, and material warping can help explain why particles in the 31.2% and 34.5% volume fractions deviated from a hydrostatic stress state as indicated by both $\Delta(R1 - R2)$ splitting and fracture results.

### 4.5.4 PS Coefficient for 21.0%, 31.2%, and 34.5% Volume Fraction Nanocomposites in Tension

A linear trend line was applied to the linear region of the R1 PS effect results for each of the volume fractions. Since it is known that the linear PS region corresponds to the linear elastic region of the material, Hooke's Law can be used to determine the PS effect with respect to stress. The corresponding applied stress was calculated using the FBG measured strain through Hooke's Law and theoretical elastic modulus. Using the error in the linear regression trend line, a range of PS coefficients were determined for each of the volume fractions as shown in Figure 4.12 and Table 4.2.

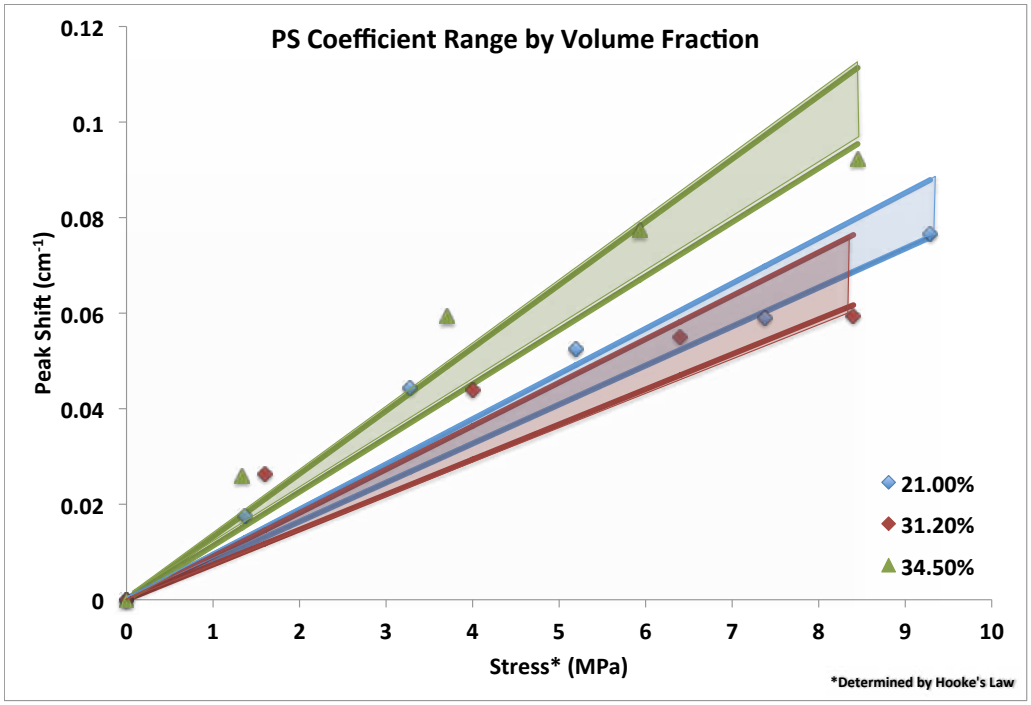


Figure 4.12: PS Coefficient Range for 21.0%, 31.2%, and 34.5% Nancomposites in Tension

Table 4.2: PS Coefficient Range by Volume Fraction in Tension

| Volume Fraction of Alumina | R1 PS Coefficient Rangle ($cm^{-1}/GPa$) |
|---|---|
| 21.0% | 8.2 - 9.5 |
| 31.2% | 7.3 - 9.1 |
| 34.5% | 11.3 - 13.2 |

The R1 PS coefficient range for 21.0% volume fraction was determined to be 8.2 - 9.5 $cm^{-1}/GPa$, 7.3 - 9.1 $cm^{-1}/GPa$ for 31.2% volume fraction, and 11.3 - 13.2 $cm^{-1}/GPa$ for 34.5% volume fraction. From Figure 4.12, it is concluded that the PS coefficient for alumina nanocomposites in tension increases with increasing volume fraction. These results are supported by previous compression results which showed that increasing the volume fraction of alumina nanoparticles in a nanocomposite increases the PS coefficient.

### 4.5.5 Comparison With Compression Results

Based on previous PS coefficient results for polycrystalline alumina, it was expected that the PS coefficient for alumina-nanocomposites with the same volume fraction of alumina nanoparticles would be the same in tension as in compression. A comparison between the R1 PS coefficient range of alumina nanocomposites in tension and the R1 PS coefficient of alumina nanocomposites of similar volume fractions in compression [44, 1] is shown in Table 4.3. In compression, the R1 PS coefficient for 21.0% volume fraction of alumina nanoparticles would be between 3.34 and 3.65 $cm^{-1}/GPa$, however, the R1 PS coefficient range for 21.0% volume fraction in tension was determined to be 8.7 - 9.7 $cm^{-1}/GPa$. For the 31.2% volume fraction, the R1 PS coefficient in compression would be between 3.8 and 3.91 $cm^{-1}/GPa$, however, the R1 PS coefficient range in tension was determined to be 7.6 - 9.4 $cm^{-1}/GPa$. For the 34.5% volume fraction the R1 PS coefficient in

compression would be between 3.8 and 3.91 $cm^{-1}/GPa$, however, the R1 PS coefficient range in tension was determined to be 11.2 - 13.2 $cm^{-1}/GPa$. Due to the increase in the tensile R1 PS coefficients in comparison to similar volume fractions in compression, it is observed that the alumina nanoparticles within the nanocomposite under these tensile experiments experienced greater load transfer than in compressive experiments. The tensile R1 PS coefficient for 21.0% volume fraction nanocomposite is about 2.4 - 2.9 times greater than in compression, 2 - 2.5 times greater than in compression for 31.2% volume fraction nanocomposites, and 2.8 - 3.5 times greater than in compression for a 34.5% volume fraction nanocomposite. The difference in the R1 PS coefficient range in tension as compared to its comparable compressive counterpart may be due in part to the challenges of manufacturing an alumina nanocomposite dogbone specimens. The complex geometry of dogbone shaped specimens along with a ceramic-like material, such as alumina-epoxy, make the machining of these specimens very challenging. Water-jet cutting, a common method for machining ceramic-like specimens, can cause jagged edges in alumina nanocomposites of low volume fractions. These jagged edges can induce micro cracks or stress concentrations which can affect the overall performance of the specimen under mechanical loading. In the case of alumina nanocomposites, alternative sample geometries are suggested, such as those utilized in a four point bending test, in order to avoid inherent manufacturing issues.

Table 4.3: Comparison of Compression and Tensile PS Coefficient Magnitude Ranges

| Volume Fraction of Alumina | R1 PS Coefficient Range ($cm^{-1}/GPa$): Compression | R1 PS Coefficient Range ($cm^{-1}/GPa$): Tension |
|---|---|---|
| 5% | 3.16 | - |
| 15% | 3.34 | - |
| 21.0% | - | 8.2 - 9.5 |
| 25% | 3.34 | - |
| 28% | 3.34 | - |
| 31.2% | - | 7.3 - 9.1 |
| 34.5% | - | 11.3 - 13.2 |
| 35% | 3.91 | - |
| 38% | 5.63 | - |

# CHAPTER 5
# APPLICATION OF A CARBON-FIBER ALUMINA STRUCTURAL COMPOSITE USING PSLS

## 5.1 Experimental Objectives

In recent years, the aerospace industry has started to use carbon fiber to manufacture aircraft components due to their low weight, high-fracture toughness, high strength, and superior insulating properties [45]. To demonstrate the application of structural composites with stress sensing capabilities, alumina nanoparticles were integrated into the manufacturing of a carbon fiber composite specimen. Using the PL response of the embedded alumina nanoparticles, the stress-sensing potential of this composite was studied.

## 5.2 Background

### 5.2.1 Carbon Fiber-Alumina Composites

The use of alumina nanoparticles as filler material has been shown to improve the mechanical properties of fiber reinforced composites [45, 46]. The presence of alumina particles was determined to increase the roughness of the fibers without damaging the fiber surface and strengthened the interfacial bonding at the fiber matrix [45]. The roughness and strong interfacial adhesion improved the flexural and interlaminar shear strength

of the carbon fiber reinforced polymer (CFRP) composite [45]. In a different study by Callender [47], an alumina coating was applied by pressing and firing alumina powder onto carbon fiber tows. Scanning electron microscopy (SEM) images revealed that the alumina coating was uniformly distributed and lacked evidence of cracks, voids, bridging or peel back.

### 5.2.2 Structural Health Monitoring Methods for Carbon Fiber Composites

Several methods have been proposed for the structural health monitoring of carbon-fiber reinforced polymer (CFRP) composites. Unlike metals, composites do not always show internal damage due to impact. Therefore, the ability to evaluate barely visible impact damage (BVID) is a major obstacle that composites face for further uses in the aerospace industries [48, 49]. Two methods that are currently in development that take advantage of the inherent 'stress-sensing' properties of carbon fiber include pulse thermography (the use of carbon fiber's thermal response) and a method that utilizes the electrical resistance of carbon fiber. For pulse thermography, the material is heated with a thermal pulse and then allowed to cool. As the pulse diffuses through the material [49], defective areas will create a heat pocket at the defect locations [49]. During the cooling transient, thermal images are collected [50]. One of the major challenges with the use of thermography is the ability to distinguish impact damage from inclusion or holes. The results of the study

by Pawar, demonstrated the ability to use thermography to detect damage at a depth of 3.2 mm from the surface of the carbon fiber laminate [49].

Monitoring changes in the electrical conductance (or resistance) of a carbon fiber panel through the individual fibers can also be used to detect damage [51, 48]. In a study by Swait, a carbon fiber panel with an integrated flexible printed circuit board was successfully used to detect and locate the damage through measurable changes in the resistance of a CFRP composite after the introduction of a BVID [48]. Swait [48] determined that the greatest sensitivity to damage was achieved when the contacts were embedded in plies adjacent to the back face of the laminate and that damage was successfully detected in panels up to 1 meter in length.

### 5.2.3 Stress-Sensing Capability of Alumina Nanoparticles

Alumina nanoparticles have been used as stress sensors during a lap shear test and coating applications. A single lap shear test demonstrated the ability to use the photoluminescence of alumina particles to provide a non-destructive method to monitor changes in stress distribution within adhesives [1]. The results of these tests verified the capability of real-time monitoring of adhesives through fiberglass substrates [1]. Several studies have been conducted to demonstrate the capability of using alumina nanoparticles as stress sensors when applied as a composite coating. In one study by Freihofer, Fugon-Dessources, et. al, plasma-sprayed alumina was applied as a coating to variable aluminum

substrate thicknesses [35]. For the first time, the spectral maps of the coatings demonstrated the ability to use PS properties of a plasma-sprayed alumina coating to detect microstructural changes in a coating responding to a mechanically loaded substrate [35]. In another study by Freihofer [52], an alumina epoxy coating was able to show damage surrounding a hole in a substrate at 77% of the failure load, where as visible damage was noted at 93% failure load. For the purposes of this study, the stress-sensing capability of embedded alumina nanoparticles in a CFRP will be demonstrated.

## 5.3 Manufacturing of Carbon Fiber Alumina Specimen

The carbon fiber specimen was manufactured using an in-autoclave process. A prescribed amount of alumina nanoparticles was added to the epoxy to yield a 5% volume fraction of alumina in the epoxy. The epoxy and alumina nanoparticles were mixed in a centrifugal mixer for 2 minutes at 2000 revolutions per minutes (rpm) followed by another 2 minutes at 2200 rpm. The particle-epoxy mixture was then manually applied to dry carbon-fiber. The specimen was placed between a release mat and an aluminum plate then bagged with a silicone matting to evenly distribute pressure that was applied by vacuum. The pressure from the vacuum forced the resin through each ply to distribute the resin throughout the laminate. To remove volatiles and off-gasses the vacuum pressure was applied for 4.5 hours. The carbon fiber alumina specimen was cut to size using a band saw. End tabs were added to the specimen to improve gripping, eliminate slipping, and evenly distribute

the gripping force. Figure 5.1 shows the carbon-fiber specimen with embedded alumina nanoparticles and Table 5.1 shows the specimen specifications.

Figure 5.1: Carbon Fiber Specimen with Embedded Alumina Nanoparticles

Table 5.1: Carbon Fiber Alumina Specimen Specifications

| | |
|---|---|
| Alumina Volume Fraction in Epoxy (%) | 5% |
| Length (mm) | 100 |
| Width (mm) | 10.07 |
| Thickness (mm) | 1.4 |
| Cross-Sectional Area ($mm^2$) | 14.1 |

## 5.4 Experimental Instrumentation

A portable spectrometer system, which is currently under development, is a novel system specifically designed to facilitate field measurement. The optical data is captured by the spectrograph, Acton SP 2156 with a grating of 1200 $l/mm$, and then digitized by the Charge-Couple Device (CCD), Pixis 100B. The laptop computer used was equipped with software that allows for the synchronization between of the XYZ stage movements and the spectrograph collection. The optical probe was mounted on the XYZ stage which was attached to an adjustable height tripod. The $Cr^{3+}$ inherent to the alumina nanoparticles were excited using an argon laser of 532 $nm$ wavelength and approximately 17 $mW$ of power at the exit of the probe. The complete experimental setup is shown in Figure 5.2.

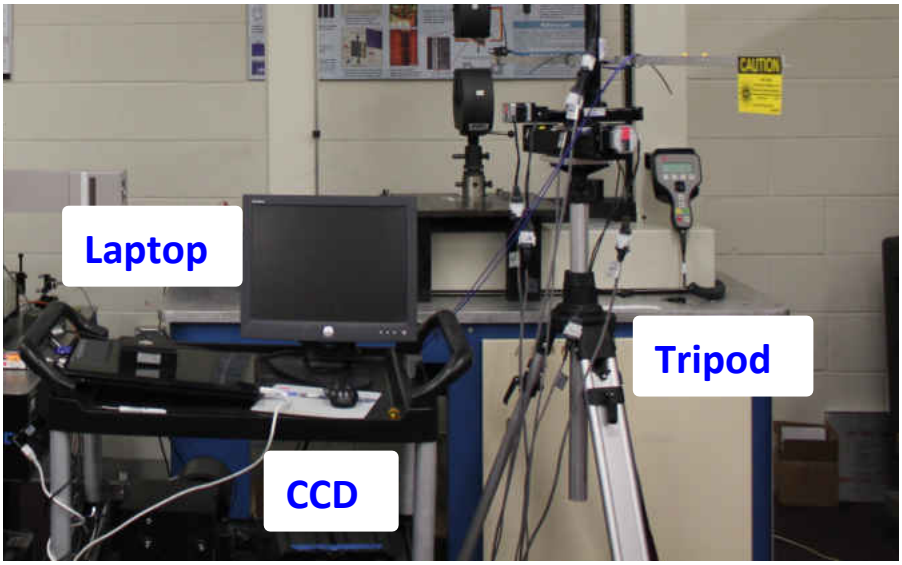


Figure 5.2: Carbon Fiber Experimental Setup

## 5.5 Data Collection Methodology

### 5.5.1 PL Data Collection

The specimen was loaded in incremental load values of 500 $N$ and held static for 1 minute. At each hold, a spectral map of 6 X 6 points encompassing an area of 2mm X 2mm was scanned using the snake scan method as shown in Figure 5.3. Each data point in the spectral map was obtained with an exposure time of 1 second with 1 accumulation.

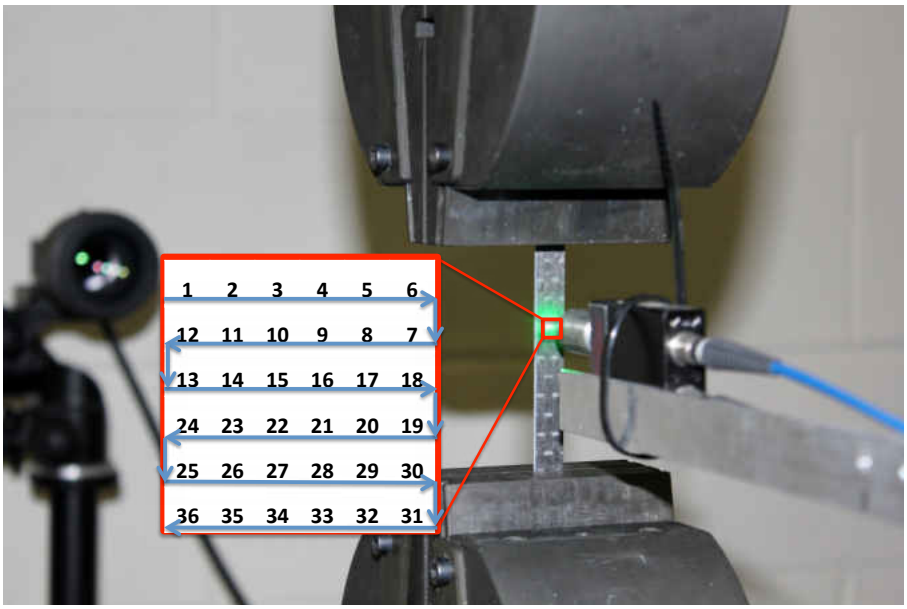


Figure 5.3: Snake Scan Method of 36 Point Map

### 5.5.2 DIC Strain Measurements

Along with collecting PL data on the front side of the specimen, Digital Image Correlation (DIC) data was collected to measure the strain on the back side of the sample to correspond to the mapped area where PL data was collected. The DIC method compares two images, pixel by pixel, collected at different times. The change in the relative position of each pixel is then converted to an average strain [53, 54]. Figure 5.4 shows the applied DIC speckles on the back side of the carbon fiber alumina specimen.

Figure 5.4: DIC Speckles on the Carbon Fiber Alumina Specimen

## 5.6 Results and Discussion

### 5.6.1 Particle Dispersion

In the development of stress-sensing structures that utilize PSLS, the ability to obtain a photo-luminescent response from alumina nanoparticles embedded in a CFRP must be shown. Figure 5.5 shows the PL response from four points within the mapped area of the specimen. Furthermore, Figure 5.5 shows that even at a very low PL intensity response, the peaks of the R-lines are discernible from noise. One of the advantages of the high-resolution capability of the PSLS method is the ability to monitor particle dispersion by monitoring the intensity of the PL response. Previous findings for intensity variance to determine particle dispersion demonstrated that increasing the volume fraction of alumina nanoparticles increases the intensity of the PL response when all excitation parameters are held constant [1]. From Figure 5.5 it can be determined that the variation of intensity values of the PL response at these four points indicates changes in particle concentration or dispersion.

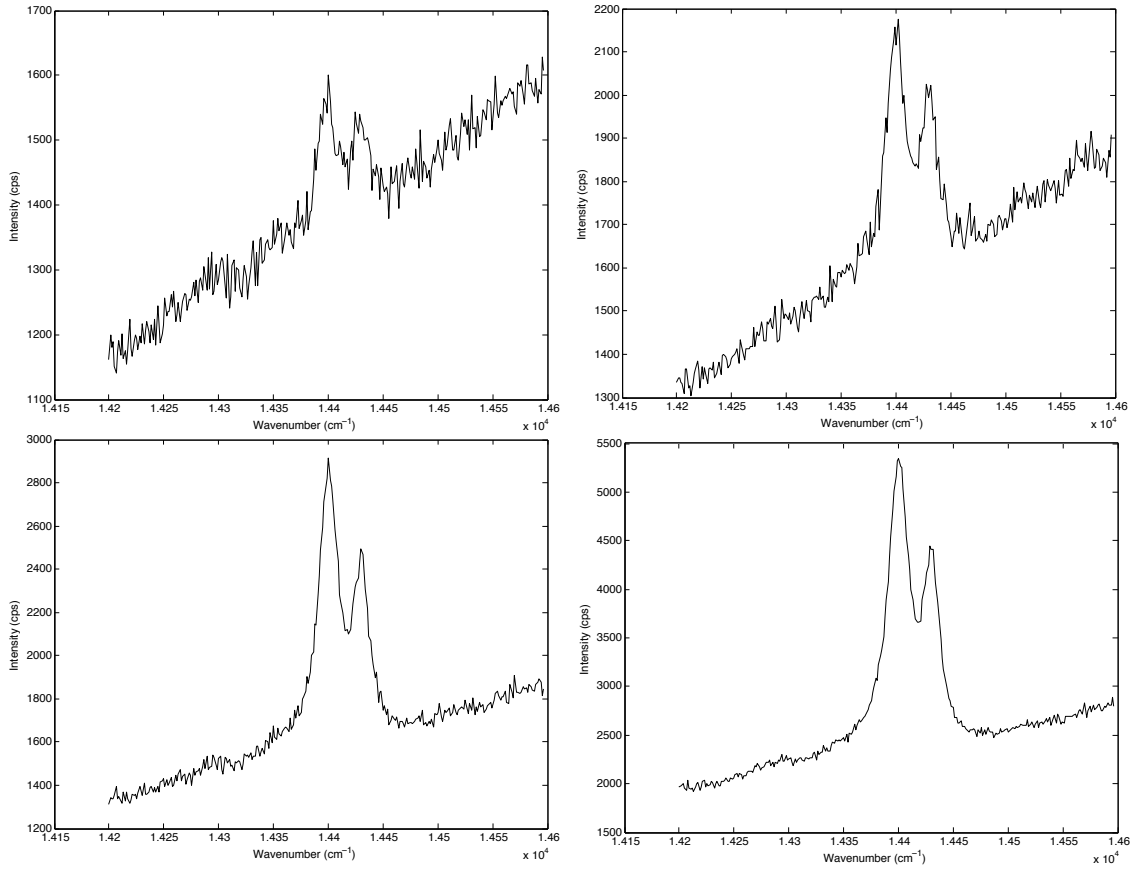


Figure 5.5: Embedded Alumina PL Intensity Results

### 5.6.2 Stress-Sensing Potential

The PL data for all 36 points within the mapped region was post-processed using the same GA procedure described in Chapter 3. The zero-load spectral map R1 peak positions were used as the reference positions from which successive peak shifts were measured.

Spectral peak shifts and corresponding strain (calculated from DIC) measurements are shown in Figure 5.6 with respect to an increasing load. As shifts in the R-lines are known to occur as a result of changes in stress (or strain), the micro-scale behavior experienced by embedded alumina nanoparticles can be detected when these particles are embedded in a carbon fiber composite as shown in Figure 5.6. The spectral maps obtained from the carbon fiber alumina specimen at increasing tensile loads contain detailed information regarding the changes in the state of stress of the alumina nanoparticles within the mapped region. Figure 5.6 shows that as the tensile load was increased, there is a variation in the R1 peak position and thus, peak shift, indicating changes in the state of stress of the alumina nanoparticles at each static load. Furthermore, the spectral maps obtained from the embedded alumina nanoparticles show the capability of the PSLS method to detect changes in strain at the micro scale as compared to the macro scale strain determined from the DIC method. The ability to use spectral information from embedded alumina particles for monitoring changes in the stress of a carbon-fiber material is a novel finding that motivates the development of stress-sensing structural composites.

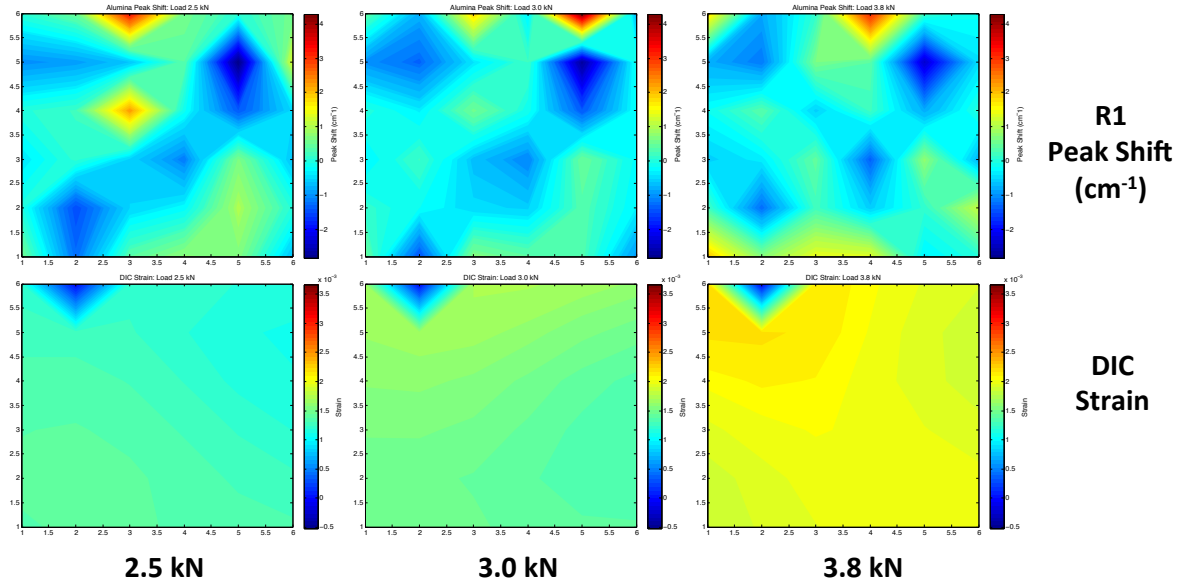


Figure 5.6: Top Row: Peak Shift with Increasing Applied Load, Bottom Row: DIC Strain Field with Increasing Applied Load

# CHAPTER 6
# CONCLUSIONS

## 6.1 Summary of Results

Due to the increased use of composites, a need for the development of a stress-sensing method for these composites was identified. In addition to showing excellent PL properties, alumina nanoparticle modifiers have been shown to improve the mechanical properties of epoxy. The piezospectroscopic method calibrates the frequency shifts of alumina's characteristic R-lines to an applied stress through the PS coefficient. While the calibration of the PS effect of alumina nanocomposites has been successfully shown in compression, the calibration of the PS effect in tension remained undeveloped.

In this study, the PS effect for an alumina nanocomposite was calibrated in tension by determining the PS coefficient range for variable volume fraction alumina nanocomposites. The PS results revealed that in tension, a linear region which is defined by the elastic limit exists followed by a region of non-linearity. The elastic limit in the PS effect was determined to be the point at which the micromechanics of alumina nanocomposites begin to significantly influence the load transfer to the alumina nanoparticles. Within the linear region, the PS coefficient range for R1 was determined to be 8.2 - 9.5 $cm^{-1}/GPa$ for a 21.0% volume fraction of alumina nanocomposite, 7.3 - 9.1 $cm^{-1}/GPa$ for a 31.2% volume fraction, and 11.3 - 13.2 $cm^{-1}/GPa$ for a 34.5% volume fraction. These results indicated that the R1 PS coefficients of alumina nanocomposites with similar volume

fractions are more sensitive in tension than in compression. The splitting of the R1 and R2 response revealed the sensitivity of tensile specimens to the inherent manufacturing challenges of alumina nanocomposites.

This PS technique was demonstrated through the application of a structural composite with stress sensing capabilities by embedding alumina nanoparticles into a carbon fiber composite. The results of this study demonstrated the capability of obtaining a photoluminescence response from alumina nanoparticles embedded in a carbon fiber composite and furthermore, the ability to determine changes in the PL response of alumina nanoparticles due to increasing tensile load. However, the challenges of manufacturing a carbon fiber alumina composite were also evident by the varying PL intensity response from the alumina particles.

By revealing the manufacturing challenges of alumina nanocomposites as well as carbon fiber composites, improvements such as alternative tensile specimens, improving particle to matrix adhesion, and improving particle dispersion can be suggested. The calibration results presented in this work of the stress-sensing capabilities of varying volume fractions of alumina nanocomposites in tension indicate a need for improvements in methods of tensile studies and sample manufacturing in the future for the development of this novel stress-sensing method.

# LIST OF REFERENCES


[1] A. Stevenson, "Calibration of alumina-epoxy nanocomposites using piezospectroscopy for the development of stress-sensing adhesives," Master's thesis, University of Central Florida, 2011.

[2] Z. Wang, F. Liu, W. Liang, and L. Zhou, "Nanoscale analysis of tensile properties and fracture of nanoreinforced epoxy polymer using micromechanics," *Journal of Reinforced Plastics and Composites*, vol. 32, pp. 1224–1233, 2013.

[3] H. Zhang, L. Tang, G. Liu, D. Zhang, L. Zhou, and Z. Zhang, "The effects of alumina nanofillers on mechanical properties of high-performance epoxy resin," *Journal of Nanoscience and Nanotechnology*, vol. 10, pp. 7526–7532, 2010.

[4] S. Zhao, L. S. Schadler, R. Duncan, and H. H. andTommaso Auletta, "Mechanisms leading to improved mechanical performance in nanoscale alumina filled epoxy," *Composites Science and Technology*, vol. 68, pp. 2965–2975, 2008.

[5] K. Dassios and C. Galiotis, "Fluorescence studies of polycrystalline $Al_2O_3$ composite constituents: piezo-spectroscopic calibration and applications," *Applied Physics A. Materials Science & Processing*, vol. 79, pp. 647–659, 2004.

[6] L. Grabner, "Spectroscopic technique for the measurement of residual stress in sintered $Al_2O_3$," *Journal of Applied Physics*, vol. 49, no. 5, pp. 580–583, 1978.

[7] S. Raghavan and P. K. Imbrie, "Ex-situ stress measurements in polycrystalline ceramics using photo-stimulated luminescence spectroscopy and high-energy x-rays," *The American Ceramic Society*, vol. 11, pp. 1–7, 2009.

[8] Q. Ma and D. R. Clarke, "Stress measurement in single-crystal and polycrystalline ceramics using their optical fluorescence," *Journal of the American Ceramic Society*, vol. 76, no. 6, pp. 1433–1440, 1993.

[9] J. He and D. R. Clarke, "Determination of the piezospectroscopic coefficients for chromium doped sapphire," *Journal of American Ceramic Society*, vol. 78, no. 5, pp. 1347–1353, 1995.

[10] S. Raghavan and P. Imbrie, "The piezospectroscopic effect of vibronic sidebands in the emission spectrum of ruby and their contribution to 3d stress measurement." Unpublished.

[11] A. Jones, "Low strain rate studies of alumina-epoxy composites using piezospectroscopy," Master's thesis, University of Central Florida, 2013.

[12] B. J. Ash, R. W. Siegel, and L. S. Schadler, "Mechanical behavior of alumina/poly(methyl methacrylate) nanocomposites," *Macromolecules*, vol. 37, pp. 1358–1369, 2004.

[13] H. Etemadi and A. Shojaei, "Characterization of reinforcing effect of alumina nanoparticles on novlan phenolic resin," *Polymer Composites*, 2013.

[14] B. Wetzel, P. Russo, F. Haupert, and K. Friedrich, "Epoxy nanocomposites-fracture and toughening mechanisms," *Engineering Fracture Mechanics*, vol. 73, pp. 2375–2398, 2006.

[15] B. J. Ash, D. F. Rogers, C. J. Wiegand, L. S. Schadler, R. W. Siegel, B. C. Benicewicz, and T. Apple, "Mechanical properties of $Al_2O_3$/polymethylmethacrylate nanocomposites," *Polymers Composites*, vol. 23, pp. 1014–1025, 2002.

[16] S. H. Lim, K. Y. Zeng, and C. B. He, "Morphology, tensile and fracture characteristics of epoxy-alumina nanocomposites," *Materials Science and Engineering A*, vol. 527, pp. 5670–5676, 2010.

[17] B. Wetzel, F. Haupert, and M. Q. Zhang, "Epoxy nanocomposites with high mechanical and tribological performance," *Composites Science and Technology*, vol. 63, pp. 2055–2067, 2003.

[18] S. Zhao, L. Schadler, H. Hillborg, and T. Auletta, "Improvements and mechanisms of fracture and fatigue properties of well-dispersed alumina/epoxy nanocomposites," *Composites Science and Technology*, vol. 68, pp. 2976–2982, 2008.

[19] H. H. Kausch and G. H. Michler, "Effect of nanoparticle size and size-distribution on mechanical behavior of filled amorphous thermoplastic polymers," *Journal of Applied Polymer Science*, vol. 105, pp. 2577–2587, 2007.

[20] E. N. Gilbert, B. S. Hayes, and J. C. Seferis, "Nano-alumina modified epoxy based film adhesives," *Polymer Engineering and Science*, vol. 43, pp. 1096–1104, 2003.

[21] R. Seigel, S. Chang, A. J. Stone, P. Ajayan, R. W. Doremus, and L. Schadler, "Mechanical behavior of polymer and ceramic matrix composites," *Scripta Materiala*, vol. 44, pp. 2061–2064, 2001.

[22] L. M. McGrath, R. S. Parnas, S. H. King, J. L. Schroeder, D. A. Fischer, and J. L. Lenhart, "Investigation of the thermal, mechanical, and fracture properties of alumina-epoxy composites," *Polymer*, vol. 49, pp. 999–1014, 2008.

[23] D. E. Munson, R. R. Boade, and K. W. Schuler, "Stresswave propagation in $Al_2O_3$ epoxy mixtures," *Journal of Applied Physics*, vol. 49, pp. 4797–4807, 1978.

[24] G. H. Michler and H.-H. K.-B. von Schmeling, "The physics and micro-mechanics of nano-voids and nano-particles in polymer combinations," *Polymer*, vol. 54, pp. 3131–3144, 2013.

[25] E. Geller, ed., *Dictionary of Material Science*. McGraw-Hill, 2002.

[26] J. Jordan, K. I. Jacob, R. Tannenbaum, M. A. Sharaf, and I. Jasiuk, "Experimental trends in polymer nanocomposites-a review," *Material Science and Engineering*, vol. A 393, pp. 1–11, 2005.

[27] J. He and D. Clarke, "Determination of fibre strength distributions from bundle tests using optical luminescence spectroscopy," *Proceedings of the Royal Society A*, 1997.

[28] S. E. Molis and D. R. Clarke, "Measurement of stresses using fluorescence in an optical microprobe: Stresses around indentations in a chromium-doped sapphire," *Journal of Electronic Structure of Ceramics*, vol. 73, no. 11, pp. 3189 –3194, 1990.

[29] A. Schawlow, "Fine structure and properties of chromium fluorescence in aluminum and magnesium oxide," *Advances in Quantum Electronics*, vol. 2, pp. 50–64, 1961. .pdf ok.

[30] A. A. Kaplyanskii and A. K. Przhevuskii, "The piezospectroscopic effect in ruby crystals," *Soviet Physics - Dokaldy*, vol. 7, pp. 313–316, July 1962.

[31] R. A. Forman, G. J. Piermarini, J. D. Barnett, and S. Block, "Pressure measurement made by the utilization of ruby sharp-line luminescence," *Science*, vol. 176, pp. 284–285, 1972.

[32] J. He and D. R. Clarke, "Determination of the piezospectroscopic coefficients for chromium-doped sapphire," *Journal of American Ceramic Society*, vol. 78, pp. 1347–1353, 1995.

[33] J. He and D. R. Clarke, "Polarization dependence of the $Cr^{3+}$ R-line fluorescence from sapphire and its application to crystal orientation and piezospectroscopic measurement," *Journal of the American Ceramic Society*, vol. 80, pp. 69–78, June 1997.

[34] S. Raghavan, P. Imbrie, and W. Crossley, "The spectral analysis of R lines and vibronic sidebands in the emission spectrum of ruby using genetic algorithms," *Applied Spectroscopy*, vol. 62, pp. 759–765, 2008.

[35] G. Freihofer, D. Fugon-Dessources, E. Ergin, A. Van Newkirk, A. Gupta, S. Seal, A. Schulzgen, and S. Raghavan, "Piezospectroscopic measurements capturing the evolution of plasma spray-coating stresses with substrate loads.," *ACS Applied Materials and Interfaces*, 2014.

[36] E. Williams and W. Crossley, "Empirically derived population size and mutation rate guidelines for a genetic algorithm with uniform crossover," in *Soft Computing in Engineering Design and Manufacturing*, 1998.

[37] W. Crossley and E. Williams, "A study of adaptive penalty functions for constrained genetic algorithm-based optimization," in *AIAA meeting papers*, 1997.

[38] J. F. Kielkopf, "New approximation to the voigt function with applications to spectral-line profile analysis," *Journal of the Optical Society of America*, vol. 63, pp. 987–995, 1973.

[39] G. Wertheim, M. Butler, K. West, and D. Buchanan, "Determination of the gaussian and lorentzian content of experimental line shapes," *Review of Scientific Instruments*, vol. 45, pp. 1369–1371, 1974.

[40] P. D. Horn and Y. M. Gupta, "Wavelength shift of the ruby luminescence R-lines under shock compression," *Applied Physics Letters*, vol. 49, no. 14, pp. 856–858, 1986.

[41] A. D. Kersey, M. A. Davis, H. J. Patrick, M. LeBlanc, K. P. Koo, C. G. Askins, M. A. Putnam, and E. J. Friebele, "Fiber grating sensors," *Journal of Lightwave Technology*, vol. 15, pp. 1442–1463, 1997.

[42] E. Neilson and R. Landel, *Mechanical Properties of polymers and composites*. Marcel Dekker, 1994.

[43] X. A. Shen and Y. M. Gupta, "Effect of crystal orientation on ruby $R$-line shifts under shock compression and tension," *Physical Review B*, vol. 48, no. 5, pp. 2929–2940, 1993.

[44] E. Ergin, "Development of nanoparticle piezospectroscopy for in-situ health monitoring," Master's thesis, Chalmers University of Technology, 2012.

[45] M. Hussain, A. Nakahira, and K. Niihara, "Mechanical property improvemnt of carbon fiber reinforced epoxy composites by $Al_2O_3$ filler dispersion," *Material Letters*, vol. 26, pp. 185–191, 1996.

[46] Y. Arao, S. Yunitori, H. Suzuki, T. Tanaka, K. Tanaka, and T. Katayama, "Mechanical properties of injection molded carbon fiber polypropylene composites hybridized with nanofillers," *Composites*, vol. 55, pp. 19–26, 2013.

[47] R. L. Callender and A. R. Barron, "Novel route to alumina and aluminate interlayer coatings for sic, carbon, and kevlar," *Journal of Material Research*, vol. 15, pp. 2228–2237, 2000.

[48] T. Swait, F. Jones, and S. Hayes, "A practical structural health monitoring system for carbon fibre reinforced composite based on electrical resistance," *Composites Science and Technology*, vol. 72, pp. 1515–1523, 2012.

[49] S. Pawar and K. Peters, "Through-the-thickness identification of impact damage in composite laminates through pulsed phase thermography," *Measurement Science and Technology*, vol. 24, 2013.

[50] X. Maldague, "Introduction to ndt by active infrared thermography," *Material Evalutions*, vol. 60, pp. 1060–1073, 2002.

[51] A. Todoroki, M. Tanaka, and Y. Shumamura, "Measurement of orthotropic electric conductance of cfrp laminates and analysis of the effect on delamination monitoring with an electric resistance change method.," *Composite S*, vol. 62, pp. 619–628, 2002.

[52] G. Freihofer, A. Gupta, A. V. Newkirk, S. Seal, and S. Raghavan, "Optical stress sensing alumina nanocomposite coatings for aerospace structures," *AIAA SciTech: 55th AIAA/ASMe/ASCE/AHS/SC Structures, Structural Dynamics, and Materials Conference*, 2014.

[53] P.-C. Hung and A. S. Voloshin, "In-plane strain measurement by digital image correlation," *Journal of the Brazilian Society of Mechanical Sciences and Engineering*, vol. XXV, pp. 215–221, 2003.

[54] F. Hild and S. Roux, "Digital image correlation: from displacement measurement to identification of elastic propertiesa review," *Strain*, vol. 42.2, pp. 69–80, 2006.